Uncertainty in strain-rate from field measurements of the geometry, rates and kinematics of active normal faults: implications for seismic hazard assessment

Claudia Sgambato[a*], Joanna P. Faure Walker[a], Gerald P. Roberts[b]

[a] Institute for Risk and Disaster Reduction, University College London, Gower Street, London, WC1E 6BT, UK

[b] Department of Earth and Planetary Sciences, Birkbeck, University of London, Malet Street, London, WC1E 7HX, UK

* Corresponding author: e-mail address: claudia.sgambato.17@ucl.ac.uk

Keywords: Active normal fault; Fault geometry; Strain-rate; Seismic hazard; Italy

Abstract

Multiple measurements of the geometry, kinematics and rates of slip across the Auletta fault (Campania, Italy) are presented, and we use these to determine: (1) the spatial resolution of field measurements needed to accurately calculate a representative strain-rate; (2) what aspects of the geometry and kinematics would introduce uncertainty with regard to the strain-rate if not measured in the field. We find that the magnitude of the post last-glacial maximum throw across the fault varies along strike. If such variations are unnoticed, different values for a representative strain-rate, hence different results in seismic hazard calculations, would be produced. To demonstrate this, we progressively degrade our dataset, calculating the implied strain-rate at each step. Excluding measurements can alter strain-rate results beyond 1σ uncertainty, thus we urge caution when using only one measurement of slip-rate for calculating hazard. We investigate the effect of approximating the throw profile along the fault with boxcar and triangular distributions and show that this can underestimate or overestimate the strain-rate, with results in the range of 72-237% of our most detailed strain-rate calculation. We discuss how improved understanding of the potential implied errors in strain-rate calculations from field structural data should be implemented in seismic hazard calculations.

1. Introduction

Fault traces and slip-rates are vital input parameters for seismic hazard assessment because they are principal controls on the location and recurrence rate of earthquakes. Fault data are currently used in some probabilistic seismic hazard assessment (PSHA) studies (e.g. Field et al., 2014; Pace et al., 2006, 2014; Peruzza et al., 2011; Valentini et al., 2017). However, detailed structural data – including variations in strike, dip, slip-vector orientation and

52 magnitude across fault bends and relay zones – are commonly not available, either due to
53 lack of detailed studies or because there are insufficient suitable locations for such data
54 collection, and hence are not included in PSHA calculations. Instead, the calculations rely on
55 planar fault geometries with a single slip-rate and slip-vector representing the whole fault. In
56 reality, mapped fault traces show variable geometry, and slip-rates change along the lengths
57 of individual faults because they are influenced by local structural complexity (e.g. Faure
58 Walker et al., 2009, 2015; Wilkinson et al., 2015). Recently, it has been demonstrated that
59 excluding such changes in geometry and slip-rates along a fault is detrimental to calculations
60 of earthquake recurrence intervals and ground shaking (Faure Walker et al., 2018), but the
61 question of what data resolution is required has not been quantified, prompting the current
62 study.
63 In detail, it has been shown that bends in faults are sites of anomalously high multi-
64 earthquake throw-rates (e.g. Gupta and Scholz, 2000; Kendrick et al., 2002; Taylor et al.,
65 2004; Faure Walker et al., 2009, 2015, 2018; Shen et al., 2009; Wilkinson et al., 2015) and
66 anomalously high coseismic throws (Mildon et al., 2016a, Wilkinson et al., 2015; Iezzi et al.,
67 2018). Variations in deformation rates along strike can result from linkage through
68 interaction and propagation of smaller fault segments (Ellis and Dunlap, 1988; Peacock and
69 Sanderson, 1994; Cartwright et al., 1995; Childs et al., 1995; Gupta and Scholz, 2000;
70 McLeod et al., 2000), and down-dip segmentation can introduce further complexity (e.g.
71 Foxford et al., 1998). Previous papers that quantified the relationship between strike, dip and
72 throw-rate, given knowledge of the kinematics, show that the throw along a fault, although in
73 general declining from a maximum value towards fault tips (Cowie and Roberts, 2001), is
74 highly variable in detail, because the fault dip and strike change in bends, causing spatial
75 variation in the way that the horizontal extension is partitioned into throw and heave along
76 strike (Faure Walker et al., 2009, Mildon et al., 2016a, Wilkinson et al., 2015; Iezzi et al.,

77 2018). Therefore, if throw-rate or slip-rate is to be used in seismic hazard to calculate mean
78 earthquake recurrence intervals for a given slip magnitude, it is important to consider values
79 of throw-rate and slip-rate in the context of changes in fault geometry and to understand the
80 implications of using just one or a couple of measurements to represent the slip-rate along an
81 entire fault (Faure Walker et al., 2018). For instance, this applies to attempts to use
82 palaeoseismology to measure slip-rate and recurrence intervals for probabilistic seismic
83 hazard analysis, when, for example, the palaeoseismology reports throw-rate or slip-rate
84 values from a single site along an entire fault. In particular we suggest that, although
85 exceptions occur (e.g. WGUEP, 2016), it is not common practice for palaeoseismologists and
86 hazard modellers' calculations to consider local variations in structural complexity (e.g.
87 changes in dip, strike, slip vector azimuth and plunge) in controlling the magnitude and
88 orientation of the slip vector. In this paper we test the hypothesis that it is desirable to have
89 multiple sites along a fault where the throw-rate or slip-rate has been constrained to capture
90 their variability, so that either a detailed model of the slip-rates along a fault or at least a
91 value that is representative can be used for inputs into hazard calculations.
92
93 In this paper, we choose a well-exposed fault in the Southern Apennines to show how the
94 geometry, kinematics and rates of deformation vary along its length, due to fault structural
95 complexity. We present detailed measurements of the fault strike, dip, slip vector and throw,
96 collected at a scale that reflects the natural variability of the fault (approximately every 1 m
97 for the fault geometrical parameters (strike and dip), 146 kinematics measurements, collected
98 at 15 sites with spacing between 10 and 50 m, and throw measurements with spacing of the
99 order of 10^2 m), and calculate the strain-rate across the fault, using our detailed throw-rate
100 profile, following a method by Faure Walker et al. (2009, 2012, 2015, 2018). We then
101 compare the results to those obtained using degraded datasets, to verify the influence of fault

geometry and local throw-rate variations on the strain-rate. We investigate what data resolution is needed to determine a deformation rate that is representative of the fault and analyse the importance of different scales of observations for calculating the strain-rate. We argue that variations in fault geometry should be considered at a scale even more detailed than what previously demonstrated, in particular when interpreting palaeoseismological data for PSHA.

2. Geological background

The Apennines are a fold and thrust belt developed during the Neogene and Quaternary, due to the convergence between the Eurasian and African tectonic plates (Anderson and Jackson, 1987; Doglioni, 1993). The thrust belt structures have been overprinted by ongoing extension. Thrusting ceased in the Plio-Pleistocene (Mostardini and Merlini, 1986; Patacca et al., 1990), except for in the NE where it is still ongoing close to the Adriatic coast (Patacca et al., 1990).

Present day southwest-northeast extension in the Central and Southern Apennines initiated at 2-3 Ma (Cavinato and De Celles, 1999; Roberts and Michetti, 2004; Barchi et al., 2007). The extension is associated with earthquakes of moderate and large magnitudes (M=5.5-7.0), occurring on active normal faults with NW-SE strike (Anderson and Jackson, 1987; Cinque et al., 2000).

In the Italian Apennines the surface offsets across active normal fault scarps have formed since the last glacial maximum (LGM) (12-18 ka), allowing the calculation of average throw-rates across the active faults in the Apennines over the last 15±3 kyrs (Roberts and Michetti, 2004; Papanikolaou and Roberts, 2007). During the LGM, the permanent snow limit was at about 1600-1700 m (Giraudi and Frezzotti, 1997), and periglacial conditions characterised areas not covered by ice, with intense erosion rates and scarce vegetation. During this period,

fault scarps were eroded and buried as sedimentation and erosion rates exceeded throw-rates; with the demise of the glaciation, the slope stabilized thanks to the establishment of vegetation (Allen et al., 1999), and a decrease in freeze-thaw action (Tucker et al., 2011), allowing the formation of fault scarps due to throw-rates exceeding the erosion and sedimentation rates. Thus, the cumulative effect of surface faulting earthquakes (M > ~6.0) has been preserved (Roberts, 2008). Analysis and dating of tephras showed that the scarps are covered by a superficial layer of Holocene deposits (Giraudi, 1995), deposited during and after the demise of the glaciation (Giraudi and Frezzotti, 1997). Moreover, the age of the scarps has been assessed through *in situ* cosmogenic ^{36}Cl exposure dating (Palumbo et al., 2004; Schlagenhauf et al., 2010, 2011; Cowie et al., 2017; Tesson et al., 2016; Beck et al., 2018; Tesson and Benedetti, 2019) and palaeoseismological studies (e.g. Michetti et al., 1996; Pantosti et al., 1996). These studies converge on the notion that the throws associated with these scarps are representative of the throw-rate since the demise of the LGM, that is since 15±3 ka (Roberts and Michetti, 2004).

Total throws across the major faults in the Apennines, developed since 2-3 Ma, have been measured from cross-sections, using 1:100,000 geological maps, revealing maximum values of up to 2000 m across individual faults (Roberts and Michetti, 2004; Papanikolaou and Roberts, 2007; Iezzi et al., 2019). In the Southern Apennines, when throw-rates post 15±3 ka are projected over 3 Ma to predict total throw, they produce throws comparable to those measured from cross-sections, confirming the age of fault initiation age (a range of 1.8-3.0 Ma is stated in Papanikolaou and Roberts, 2007). This also suggests that throw-rates in the Southern Apennines have been constant since the initiation of faulting (Papanikolaou and Roberts, 2007). This suggests, for the Southern Apennines, that the throw-rates over 15±3 ka are representative of longer time periods, demonstrated by a strong relationship found between calculated strain-rates over 15±3 ka and total throws developed since 2-3 Ma, which

153 also correlate with mean elevation, free air gravity data and SKS splitting delay times in the
154 mantle (Faure Walker et al., 2012). These findings suggest that the extension in the
155 Apennines is ultimately influenced by mantle upwelling and viscous flow at depth (e.g.
156 D'Agostino et al., 2011; Faure Walker et al., 2012; Cowie et al., 2013) and topography and
157 extension are the result of the uplift (Faure Walker et al., 2012; Cowie et al., 2013).
158 The study area is located in the Southern Apennines, where the NE-SW extension prevailed
159 since middle Pleistocene (Hippolyte et al, 1994; Papanikolaou & Roberts, 2007).
160 Major active faults in the Southern Apennines strike NW-SE and have a length of 20-45 km
161 (Papanikolaou and Roberts, 2007; Faure Walker et al., 2012). Moreover, most of the active
162 faults in the region have generated hangingwall basins (Maschio et al., 2005; Barchi et al.,
163 2007, Papanikolaou and Roberts, 2007; Amicucci et al., 2008), infilled by Upper Pliocene-
164 Middle Pleistocene sediments, consistent with the idea that the extension in the Southern
165 Apennines started at about 1.8-3.0 Ma (Patacca et al., 1990; Barchi et al., 2007; Papanikolaou
166 & Roberts, 2007).
167 The studied fault section (Figure 1), herein called the Auletta fault, also known as the
168 Caggiano fault (Galli et al., 2006; Spina et al., 2008), is a 3 km normal fault crossing the
169 Cretaceous carbonates of M. San Giacomo, northeast of the Auletta town. The fault borders
170 the NE side of the NW-SE trending Auletta basin (Ascione et al., 1992; Gioia et al., 2010).
171 The Auletta basin is infilled by marine and continental deposits from the Middle Pliocene to
172 Middle Pleistocene, with maximum thickness of 500 m (Amicucci et al., 2008). Seismic
173 reflection profiles across the basin show two depocentres (Amicucci et al., 2008), with a
174 major NE dipping normal fault, bordering its SW margin (Alburni Fault), that probably
175 controlled the stratigraphic and geomorphological evolution of the basin, causing the tilting
176 of the deposits in the hangingwall (Barchi et al., 2007; Amicucci et al., 2008, Gioia et al.,
177 2010). The Auletta fault forms the NW segment of the Vallo di Diano system (Figure 1),

178 indicated by throw and kinematic data that indicate how throws decreases from a maximum
179 in the Vallo di Diano, with ~SW-directed slip vector azimuth, to a minimum near the fault tip
180 at the NW end of the Auletta fault, with a ~SSW-directed slip vector azimuth (Papanikolaou
181 and Roberts, 2007; Faure Walker et al., 2012; see Figure 1). The link between the Auletta
182 fault and Vallo di Diano fault has also been suggested by other workers, since the two
183 segments are characterised by space-dependent slip variation (Spina et al., 2007; Soliva et al.,
184 2008; Villani and Pierdominici, 2010). Variations in fault slip direction can be observed
185 along the strike of active normal faults, with oblique-slip close to the fault tips (Roberts,
186 1996, 2007), in accordance with theoretical strain patterns in normal faults (Wu & Bruhn,
187 1994; Ma & Kusznir, 1995). This occurs because strain is influenced by the asymmetric
188 displacement in the fault blocks (Wu & Bruhn, 1994), caused by the smaller uplift of the
189 footwall compared to the hangingwall subsidence, determining larger strains in the
190 hangingwall compared to the footwall (Ma & Kusznir, 1995).
191 The combined Auletta and Vallo di Diano faults would suggest a total length for the main
192 structure of ~35 km; therefore, it is considered by many authors to be responsible for the
193 earthquakes in 1561 (Mw 6.3 and 6.7) (e.g. Galli et al., 2006; Barchi et al., 2007; Soliva et
194 al., 2008; Villani and Pierdominici, 2010). The lateral continuity and vertical offset of the
195 Auletta fault scarp suggest Holocene activity (Hippolyte et al., 1993; Papanikolaou &
196 Roberts, 2007), and palaeoseismological trenches confirm the recent activity (Galli et al.,
197 2006). No known event is specifically attributed to the Auletta fault in the historical
198 catalogues (although see the comments above on the 1561 earthquake); however, the high
199 seismic potential of the area is demonstrated by some of the most destructive earthquakes in
200 the Southern Apennines, such as the events occurred in 1466 (Mw=5.9), 1561 (Mw=6.3, 6.7),
201 1853 (Mw=5.6), 1857 (Mw=7.1) and 1980 (Mw=6.9) (Figure 1). The earthquake that
202 occurred on November 23rd, 1980 (Mw=6.9, CPTI15), is one of the strongest events recorded

in the Italian seismic catalogue, resulting in ~3000 fatalities and extensive damage (Westaway and Jackson, 1987). The structure responsible for the event was a complex fault ~35 km long, composed by different NW-dipping segments (Westaway and Jackson, 1987; Pantosti and Valensise, 1990), and a SW-dipping antithetic fault (Bernard and Zollo, 1989) (Figure 1). The two seismic events of July and August 1561, (Mw=6.3 and Mw=6.7, CPTI15) caused about 600 casualties and had a damage distribution suggesting that they possibly involved rupture on the Auletta fault (Galli et al., 2006; Spina et al., 2007; Castelli et al., 2008; Villani and Pierdominici, 2010; see Figure 1). Although the Val d'Agri fault is widely accepted to be responsible for the 1857 event (Mw=7.1, CPTI15) (Benedetti et al., 1998; Barchi et al., 2007; Villani and Pierdominici, 2010), it has been hypothesised that the Auletta fault generated a northern shock associated with the 1857 earthquake (Galli et al., 2006), which had the highest damage localised in the northern part of the Vallo di Diano and Val d'Agri.

3. Methods

3.1 Structural mapping

The trace of the Auletta fault was identified using geological and topographic maps at the scale 1:100,000, and mapped in Google Earth to constrain the location of the scarp to within a few meters, and constrained through fieldwork. Detailed structural mapping was undertaken on the Auletta fault (Figure 2), using a hand-held GPS with accuracy of ±5 m, to record the exact location in UTM coordinates and determine the length of the fault scarp. The SE section of the fault was mapped at a detail of ~1 m, for about 1 km (Figure 2c). However, we were unable to map across the whole fault length in such high detail, since in the central and NW sections, the scarp is highly degraded or is not continually exposed. Geomorphological

features such as gullies, scree, colluvial deposits, were also mapped as noting such features is fundamental for the characterisation of the slip-rates of faults, since geomorphic processes can contribute to the fault plane exhumation (Bubeck et al., 2015).

To understand the relationship between the geometry, kinematics and rates of deformation, we collected structural field measurements, such as fault strike, dip, slip vector azimuth and plunge, and the post 15±3 ka offset across the scarp. Geometric and kinematic data were measured using a compass clinometer, with a precision of ±2°, based on accuracy of the compass readings. The kinematics of the faulting was measured at 20 locations across the whole fault from striations and corrugation on slickensides of the fault plane, avoiding measurements within hangingwall gullies, which might be affected by mass wasting. Where these indicators were not available, the kinematics were derived from calculation of the b-axis in Stereonet 10.0 (Allmendinger et al., 2012; Cardozo et al., 2013), following the lead of Roberts (2007). In this method, the b-axis is defined by a pole to a best-fit great circle through the poles to the fault planes. Thus, the b-axis approximates the orientation of the corrugations long-axes, hence the slip-vector orientation is defined by the intersecting fault surfaces composing the main fault plane. Mean values for the slip vector azimuth and plunge were calculated for each location using a Fisher vector distribution in Stereonet 10.0, with 95% and 98% confidence intervals. The dataset described above is presented in Figure 3.

To provide an alternative representation of the geometry, kinematics and rates of deformation, the data have also been averaged along 8 sections of the fault (Figure 4), these values are also used for the strain-rate calculations (see section 3.3). These sections were chosen after careful observations of the geometrical and structural variations affecting the fault plane. To preserve the detail of the mapping in the south-east segment, the section lengths were maintained at around ~100 m. In the north-western tip of the fault the data are

253 averaged within ~250 m sections; this is due to the lack of detailed kinematic indicators in
254 this section of the fault, where the scarp is more degraded.
255
256 *3.2 Scarp profile*
257
258 In order to constrain the amount of fault offset since the demise of the LGM (Last Glacial
259 Maximum), and hence derive the rates of deformation, we produced topographic profiles
260 across the Auletta scarp. The throw, defined as the vertical component of the offset, can be
261 used to define the throw-rate since 15±3 ka, since the surface offsets across active normal
262 fault scarps in the Italian Apennines are an expression of the post LGM activity of the faults
263 (Roberts and Michetti, 2004; Papanikolaou and Roberts, 2007). However, throw-rate
264 variations along the fault are detectable at different spatial scales (Faure Walker et al., 2009,
265 2010, 2015; Wilkinson et al., 2015; Mildon et al., 2016a; Iezzi et al., 2018). Therefore, in
266 order to determine the variations in throw-rates along the fault, we produced the profiles with
267 a systematic approach, avoiding biases due to exclusion of sites of minimum throws, as often
268 sites that are more likely to be chosen are those with a higher offset. In addition, locations
269 were chosen to avoid areas of post-glacial erosion or sedimentation.
270 The profiles were measured using a 1 m ruler and clinometer to measure the slope
271 inclination. The altitude was recorded at the beginning and end of the topographic profile
272 using a barometric altimeter, which allows for instrumental precision of ±1 m; the difference
273 in altitude compared to that measured with the meter ruler was used to determine the error.
274 To assess the accuracy of our method, we compared uncertainties obtained using different
275 techniques. Differences between profiles constructed using terrestrial laser scanner and meter
276 ruler are in the order of ~10% (Faure Walker, 2010), which is significantly less than the
277 natural throw-rate variability observed along strike both in terms of cumulative (~20%,

278 Roberts and Michetti, 2004; Papanikolaou et al., 2005) and coseismic offset (~40%, Iezzi et
279 al., 2018).
280 Geomorphic features, necessary for a correct definition of the throw of the fault were also
281 noted; these are the upper slope, the degraded fault scarp, the fault plane/free face, the
282 colluvial wedge and the lower slope. The locations of these features were noted in the field
283 and then identified and interpreted on the profile; the vertical distance between the
284 projections of the upper slope and lower slope surfaces onto the fault plane define the throw.
285 We included in our dataset 5 additional scarp profiles, produced with the same methodology,
286 from previous works (Papanikolaou and Roberts, 2007; Faure Walker et al., 2012) (see
287 Figure 2b for locations). Therefore, a total of 11 measurements of throw across 3 km of the
288 Auletta fault are available (Figure 5).
289
290 *3.3 Strain-rate*
291
292 In order to understand the importance of representative throw-rate profiles at the scale of an
293 individual fault, in terms of how the geometry, kinematics and rates of deformation vary
294 across structural complexities such as along-strike fault bends, we calculate the strain-rate
295 across the Auletta fault, using all the measurements of throw, and then progressively degrade
296 the dataset, re-calculating the strain-rate for each degradation step.
297 Using our field measurements of fault strike and dip, slip vector azimuth and plunge, and
298 throw, we calculate the strain-rate, using a method developed by Faure Walker et al. (2009,
299 2010, 2012, 2018), which is an adaptation of the Kostrov (1974) equations, and modified to
300 preserve the high detail available for the Auletta fault. Table 1 provides the values used
301 within the calculations. Equation 1 (Faure Walker et al., 2010) shows how the maximum
302 horizontal strain-rate component of the strain-rate tensor is calculated:
303

$$\dot{\varepsilon}_{1'1'} = \frac{1}{2at}\sum_{k=1}^{K}\left\{L^k T^k cotp^k \left[sin(\varphi^k - \Phi^k) + sin\left(\varphi^k + \Phi^k + arctan\left(\frac{\sum_{k=1}^{K} L^k\, T^k cotp^k cos\,(\varphi^k + \Phi^k)}{\sum_{k=1}^{K} L^k\, T^k cotp^k sin\,(\varphi^k + \Phi^k)}\right)\right)\right]\right\}$$

(1)

Where $\dot{\varepsilon}_{1'1'}$ is the maximum horizontal average strain-rate tensor, Φ = strike, φ = slip direction, p = plunge, T = throw, L = length of the fault, a = surface area of the region concerned, t = time during which the total slip from all the earthquakes occurred on a given fault, k = measurements for each section of the fault within the surface area.

To assess how detailed the mapping of field parameters and the fault trace need to be so as to accurately calculate the strain-rate across such faults, we calculate the strain-rate progressively degrading the dataset, removing one location at a time. To avoid an arbitrary choice of which location to remove, we calculated all possible combinations of 10 out of 11 data points, 9 out of 11 data points, 8 out of 11 data points, etcetera. Figure 6 shows calculated strain-rates for each combination of throw measurements versus the number of throw measurements included for two different spatial resolutions; the 'all data' model which incorporates all 11 measurements of throw is represented by the single point on the right end of the plot. The ±1σ error in strain-rate, represented as a grey area, is calculated for the all data model only, since all the other models are simplified calculations using degraded data.

To calculate the strain-rate values, the fault trace was discretized on a grid with boxes of 200 m x 2 km size (Figure 6a) to allow the calculation on planar segments, whilst preserving the information on the geometrical complexity of the fault, such as bends in strike and variations in the throw and slip vector. The same was carried out using a grid with boxes of 2km x 2km size (Figure 6b), to compare the uncertainty relating to the use of different scales of

observations. The fault throw and slip vector are interpolated linearly between data points included in the calculations. The strain-rate was calculated within each grid box containing a planar segment; the strain across the whole fault is obtained by summing the strain of the boxes containing a fault segment, accounting for the change in area of the grid.

To further investigate the effect of detailed and degraded data, we compared the strain-rate calculations obtained on a regular 100 m x 2 km grid using six different scenarios of throw profiles (Figure 7): (i) the 'all data' throw profile, built using all the available data; (ii-1) the 'boxcar-max' profile, which uses the single maximum value of throw, projected along the whole fault; (ii-2) the 'boxcar-mean' profile, for which a mean value of throw is calculated from all the throw measurements and this value of throw is projected along the whole fault; (ii-3) the 'boxcar-min' profile, built extrapolating the minimum measured throw value along the fault; (iii-1) the 'max-mid-triangle' profile, built by extrapolating the maximum throw value, placed at the centre of the fault, and decreasing it to the fault tips, where the throw is considered zero; (iii-2) the 'max-point-triangle' profile, where the maximum throw value is placed in the same location where it has been measured on the fault, and decreases to zero to the fault tip.

4. Results

4.1 Structural mapping and data

The structural map of the Auletta fault (Figure 2) shows the 3 km fault scarp, with details of the fault strike, dip and slip vector. We collected a total of 433 measurements of strike and dip and 146 measurements of slip vector azimuth and plunge. The average strike value is N127°, however, the map in Figure 2b shows the high variability of strike, which is attributed to the natural corrugations affecting the fault plane both at small and large scales. The

stereographic projection in Figure 2b shows a mean slip vector value for the whole fault of 61→209, suggesting a dip-slip or slightly sinistral oblique motion, towards SSW. Moreover, the calculated b-axis value orientation is 61→203, which is almost coincident with the mean slip vector, suggesting that the individual fault planes orientations are organised in a manner that accommodates and facilitates the slip vector (Roberts, 2007).

Figure 2c shows the southeast section of the fault scarp that has been mapped in more detail. As well as showing structural data, the map describes the preservation state of the fault scarp and other geomorphological features, such as upper slope limit, lower slope limit, Holocene gullies and deposits. Five of the six scarp profiles produced for this work have been constructed in this section of the fault (blue lines in Figure 2c). Note that the location of the profiles was carefully chosen to avoid post 15±3 ka gullies and areas of sedimentation and to be well spaced so as to represent the variability of the fault parameters.

Figure 3 shows all the data collected in detail along the Auletta fault and plotted against the longitude difference between A-B (see also Figure 2b). At this scale, the high variability in strike and dip is evident. Figure 3b shows corrugations of the fault plane both at large and small scale, with variations of the strike between N070° and N152° within the ~3 km fault length, whereas the fault dip has mean values between 45° and 76° (Figure 3c). Slip vector azimuth and plunge have been measured at 21 locations along the fault, showing that the slip vector azimuth varies between N158° and N240° (Figure 3d). No clear relationship can be seen between strike and dip. Mean values for the strike, dip and slip vector azimuth have been calculated within 8 sections along the fault as described above (see section 3.1) and are shown in Figure 4. These values were also used within the calculations of strain-rates. Average values for the slip vector azimuth from point A to B are shown in Figure 4d, and these are: 212°, 170°, 215°, 199°, 203°, 208°, 223°, 202°, thus a maximum variation of 53° can be found. The maximum variation of slip vector azimuth along the Auletta fault is ~15%,

suggesting that the slip vector azimuth remains almost constant along the fault, despite the variations in strike and dip. This can be also observed in the single sites Stereonets in Figure 2c, where the slip vector is almost dip slip along the whole fault length.

4.2 Throw variations

Figure 5 shows the 11 scarp profiles across the Auletta fault. The location of each profile is shown in Figure 2b. The throw has a minimum measured value of 2.9 m, measured at the northernmost section of the fault (Figure 5, loc. 1), suggesting that at this location we are closest to the tip of the fault. The throw does not show a maximum in the centre of the fault section, because the entire fault probably includes the Vallo di Diano fault to the SE, so our data only covers the area close to the NW tip of this overall structure. For this reason, the throw progressively decreases towards northeast, from a maximum value of 10.1 m at location 11. Since we hypothesised that the Auletta fault scarp has formed since the demise of the LGM, we are able to calculate a throw-rate using our most detailed dataset. Using a weighted average throw value of 4.3 m, assuming that the throw decreases to zero at both ends of the fault trace, we derived a throw-rate of 0.28 ± 0.06 $mmyr^{-1}$ since 15±3 ka. However, note that using a maximum and minimum value of throw measured from scarp profiles on the Auletta fault, the throw-rate is as low as 0.19 ± 0.04 $mmyr^{-1}$ for a minimum value of 2.9 m, and 0.67 ± 0.14 $mmyr^{-1}$, using the maximum measured throw value of 10.1 m; thus, the rates of deformation differ by a factor of ~3.5. Values of throw and average dip have been projected against distance (longitude) in Figures 4e and 4c respectively. These figures show a relationship between the throw and dip of the fault, in particular between 2200 m and 2800 m. Although the maximum values of throw are found to the southeast end of the Auletta fault, a local increase in throw is observed at about 2200 m, where the throw has a value of 7.7 m (Figure 5, loc. 3); note that in this section the average dip has the highest value

(73°). The throw decreases to 4.8 m (Figure 5, loc. 4) over about 200 m distance (~2400 m), and this coincides with the location where the dip shows a lower value (58°). The above suggests that the throw is highly dependent on the geometry (strike and dip) of the fault.

4.3 Strain-rate calculations

With the complexity in the geometry, kinematics and rates of throw accumulation described above in mind, we calculated the implied strain-rates. These calculations of strain-rates are shown in Figure 6 and 7. The strain-rate across the Auletta fault, calculated with all the throw data collected is $6.43 \pm 1.48 \times 10^{-8}$ (Figure 6). However, we are also interested in how this value would change if we had not measured all the locations described in Figure 2, 3 and 4. Hence we progressively degraded the data as described above (see section 3.3). Not surprisingly, a convergence of the calculated strain-rates towards the all data model can be observed as more values are progressively added (Figure 6). However, we find interesting differences in the results depending on the chosen box size. For example, at the 200 m x 2 km boxes scale (Figure 6a), the only degraded models where results fall within the error margin for the 'all data' case, represented by the grey shaded area, are models that use most of the data locations, that is, at least 9 of the 11 measurement sites. Another interesting result for the 200 m x 2 km grid size, is that, for example, when using only one value of throw, the calculated strain-rate shows a high variability, with values between 2.35×10^{-8} and 7.70×10^{-8}. With strain-rates differing respectively ~2.8 and ~0.8 times the 'all data' case, these results show that using a single value is not a rigorous way to measure strain-rate.

To investigate the effect of changing the grid size, we have also calculated values for a 2 km x 2 km grid; we compare these results to the ones obtained using a grid with boxes of 200 m x 2 km described above (compare Figures 6a and 6b). Values for the strain-rate for the 'all data' scenario are similar for both grid sizes, and again we recognise a convergence towards

428 the all data model when more data points are added to the calculations in the 2 km x 2 km
429 grid. However, due to the higher error margin for the calculated all data case strain-rate in the
430 2 km x 2 km calculation, the strain-rates for the degraded data sets are within the error
431 margin of the all data set when as few as 5 values of throw are used within the calculation.
432 This suggests that independently from the scale we choose, we obtain the same result for the
433 calculated strain-rate in the 'all data' case, but the error associated with the use of a larger
434 scale (e.g. 2 km) is detrimental to the aim of understanding the system.
435 To further investigate how else the results might be misconstrued or misrepresented, we
436 compared calculations of strain-rate in a regular 100 m x 2 km grid to datasets obtained
437 degrading the data in another way, that is by imposing boxcar or triangular slip-distributions,
438 following the approach of Faure Walker et al. (2018) (Figure 7). The data of throw and slip
439 vector azimuth and plunge used in the calculation of the 'all data' case are provided in Table
440 1. Figure 7(i) shows the strain-rates calculated using all the available data. Figure 7(ii-iii)
441 show the calculated strain-rates across the Auletta fault, using 'boxcar-max', 'boxcar-mean',
442 'boxcar-min', 'max-mid-triangle' and 'max-point-triangle' throw profiles; the blue bars in
443 each graph represent the strain-rates for the 'all data' case. The results show how the strain-
444 rate changes when the datasets are degraded in this way. In particular, we observe variations
445 of the strain-rate between 237%, 105%, 72% of the 'all data' profile for the 'boxcar-max',
446 'boxcar-mean', 'boxcar-min' throw profiles respectively and 120% of the 'all data' profile
447 for the 'max-mid-triangle' and 'max-point-triangle'. Among these, the 'boxcar-max', 'max-
448 mid-triangle' and 'max-point-triangle' throw profiles analyse cases where the maximum
449 throw measurement is used. Moreover, our results show that the optimal choice for this fault,
450 that is the choice that best represents the 'all data' situation, would be the 'boxcar-mean'
451 scenario, which shows the least difference from the 'all data' case (105%). In conclusion,
452 smaller box sizes and inclusion of more data sites improves the overall strain-rate result.

5. Discussion

Many examples exist in the literature detailing the geometry and kinematics of slip across segmented normal faults (e.g. Cowie and Roberts, 2001; Cowie et al., 2001, 2012, 2013; Faure Walker et al., 2009, 2015, 2018; Shen et al., 2009; Wilkinson et al., 2015; Mildon et al., 2016a; Iezzi et al., 2018), and Faure Walker et al. (2009) was the first to provide equations that link fault parameters such as strike, dip, throw and slip vector azimuth and plunge to strain-rate using relationships derived from the Kostrov equations (Kostrov, 1974). Some of these studies have shown that throw varies systematically with the fault strike and dip, resulting in significant alterations in the implied recurrence rates and ground-shaking intensities, if values are used for probabilistic seismic hazard analysis (PSHA). Faure Walker et al. (2018) have emphasised the need for detailed measurements in terms of spatial resolution and information on variable fault geometry, when using these data in PSHA (Faure Walker et al., 2009, 2010, 2018; Wilkinson et al., 2015), yet a quantification of how detailed the measurements need to be is still an open question.

In this paper we show that variations in throw can be measured in the field at a relatively-high resolution and quantify the effect of different spatial resolutions. For example, the field data collected along the studied fault reveals a dramatic variation of throw at a local scale, with a change from 7.7 m to 4.8 m over only ~200 m distance (Figure 3e, Figure 4e). These variations are related to fault geometry; in particular, the maximum offsets occur where the dip of the fault is higher (Figure 3c, e and Figure 4c, e).

The above implies that site selection plays a fundamental role in the process to determine the throw-rate or slip-rate model for an individual fault. Indeed, we stress the importance of structural and geomorphic characterisation of the data collection sites to recognise areas where geological and geomorphological processes might have influenced the fault plane

479 exhumation, and thus where slip vector magnitude and throw measurements may be
480 impaired. Areas affected by such processes are generally found at short distance from those
481 undisturbed along the fault scarp (few tens of meters or less) (Bubeck et al., 2015; see also
482 Figure 2c). This emphasises the need for an approach that takes into consideration the
483 variability in fault parameters shown herein, as well as all the local geomorphic features that
484 might characterise the fault.
485 In particular, below we discuss the implications of (1) different sized boxes for calculating
486 strain-rate, (2) the number of measurements within each box, (3) implications for recurrence
487 intervals compared to the traditional approach of estimating a coefficient of variation for
488 recurrence intervals, and (4) inferring palaeoearthquake magnitudes from maximum
489 displacement measurements.
490
491 In terms of different sized boxes for calculating strain-rate, the results that we obtained
492 comparing two different scales for the calculation of the strain-rate (Figure 6) are indicative
493 of the need to determine a representative scale of observation, relating to the detail of data
494 available, since a larger scale will allow the use of fewer measurements of throw, but this will
495 be accompanied by an increased uncertainty in derived values, which should be carefully
496 considered within PSHA calculations. We have considered the fact that our study is of a
497 rather short fault (3 km length) whilst seismic hazard is known to be dominated by the largest
498 faults in a region (25-40 km length for the Southern Apennines; Figure 1). Thus, it would be
499 desirable to upscale our findings to comment on what detail would be needed for taking
500 measurements of the geometry, kinematics and rates of deformation on large faults. One way
501 to consider this is to upscale the grid boxes sizes with the same upscaling defined by the
502 differences in size between faults. This would imply that the results that we obtain at a 200 m
503 scale for the Auletta fault, which has a length of 3 km, can perhaps be compared to those for

504 a 30 km fault where 2 km grid boxes are used. If this is the case, then we suggest that
505 structural complexity measurements are needed at a scale smaller than 2 km for the largest
506 faults in a region like the Southern Apennines, but we suggest this needs further work to test
507 this hypothesis.
508
509 In terms of the number of measurements within each box, our results show a high variability
510 when strain-rate is calculated using just one throw measurement (Figure 6), or boxcar and
511 triangular throw profiles (Figure 7), results consistent with Faure Walker et al. (2018). In this
512 article, we confirm that for an individual fault, the strain-rate is highly affected by the local
513 changes in throw, which are strongly dependent on the fault structural complexity. Overall,
514 the results shown in Figures 6 and 7 reinforce the concept that one measurement of throw or
515 slip is inadequate to calculate the strain-rate across a fault, a result consistent with that found
516 investigating different faults in previous work (Faure Walker et al., 2018). However, we
517 noticed that the strain-rate calculated using an average throw is closer to the 'all data' case
518 ('boxcar-mean' scenario, 105% of the 'all data'), a result comparable to those obtained by
519 Faure Walker et al. (2018). This would suggest that the 'boxcar-mean' may give the best
520 results in terms of strain-rate calculations, but we highlight that the 'boxcar-mean' throw
521 value was a mean of all 11 measurements, so this simplification still requires detailed
522 knowledge (enough measurements) of throw so that the calculated strain-rate is
523 representative of the 'all data' case. Therefore, the results obtained using the 'boxcar-mean'
524 scenario should be considered carefully, since good results can be obtained only when
525 comprehensive datasets are available.
526
527 In terms of implications for recurrence intervals compared to the traditional approach of
528 estimating a coefficient of variation for recurrence intervals, our results show that using a

529 single or average throw or slip-rate value for the whole fault could lead to a large uncertainty
530 in seismic hazard calculations. Calculated strain-rates and hence implied earthquake moment
531 release rates across faults in PSHA are influenced by throw and slip variations at a local scale
532 and so fault recurrence intervals calculated using single measurements of throw or slip-rate
533 are likely to be misleading. We are aware that the Auletta fault is a short segment of a larger
534 fault, thus not capable of large earthquakes alone. However, if we assume that the same
535 relative changes in throw-rate as we observed along the Auletta fault segment can be applied
536 to the whole Vallo di Diano fault, we can hypothesise the uncertainty in recurrence interval
537 that can be obtained when using a degraded dataset, or when variations in throw-rate are not
538 recognised. Our results show that when only one measurement of throw is used across the
539 studied Auletta fault segment, the calculated strain-rates have values differing by a factor of
540 ~3.5 (Figure 6), therefore, the implied average recurrence interval for a given earthquake
541 magnitude would be about three times longer or shorter. Such a range is comparable to the
542 typical values for the average recurrence intervals of displacement events in the Central and
543 Southern Apennines, derived from palaeoseismological analyses, which are between 1000
544 and 3000 years (e.g. for the Southern Apennines: Caggiano fault:1600 yr, Galli et al., 2006;
545 Irpinia fault: 1684-3140 yr, Pantosti et al., 1993; Val d'Agri fault: 2500 yr, Benedetti et al.,
546 1998; Matese fault: 1700 yr, Galli and Galadini, 2003; Castrovillari fault: 800-2380 yr, Cinti
547 et al., 1997. For the Central Apennines: Fucino fault: 1500-2000 yr, Galadini et al., 1997;
548 1400-2600 yr, Galadini and Galli, 1999; Ovindoli-Pezza fault: 2760-3300 yr, Pantosti et al.,
549 1996; Norcia fault: 1700-1900 yr, Galli et al., 2005). The large uncertainty suggested for
550 earthquake recurrence intervals derived from palaeoseismology is typically attributed to
551 limitations in dating techniques. However, we show that an additional level of uncertainty has
552 to be considered, that is the error derived from the natural variability in displacement rates

553 along the fault. Therefore, if results from palaeoseismology are to be used to infer recurrence
554 intervals, we suggest that multiple sites along a fault are preferable.
555 The variability in average recurrence time is generally defined with the coefficient of
556 variation (CV), calculated as the standard deviation of the inter-earthquakes-time divided by
557 the mean recurrence time (CV=σ/T_{mean}). Typical values suggested for the CV are equal or
558 below 0.5 (e.g. 0.5, Ellsworth et al., 1999; 0.14-0.34, Pace et al., 2006; 0.38, González et al.,
559 2006; 0.48, Lienkaemper and Williams, 2007; 0.2-0.39, Visini and Pace, 2014), and small
560 variations in CV produce a high variability in earthquake probability forecasts (Visini and
561 Pace, 2014). However, in this work, and consistent with the results of Faure Walker et al.
562 (2018), we have determined a variation in strain-rate, and hence earthquake moment release,
563 that exceeds the uncertainty suggested by these CV. In this case, variations in slip-rate along
564 strike do not directly imply variability in earthquake recurrence through time, but they might
565 affect average recurrence interval calculations, directly related to CV. Within the same
566 temporal window, an increase in T_{mean} would determine a decrease in CV, thus the
567 uncertainty that we observe in slip-rate, and consequently in T_{mean}, would introduce a further
568 uncertainty that is beyond that typically observed in CV.
569 In addition to causing errors in calculated recurrence intervals, using a single measurement of
570 throw or slip across a fault may cause errors in inferred earthquake magnitudes. This is
571 because it is plausible that sites of maximum throw are more likely to be considered, since
572 they show higher offsets and are more easily identified. This has been pointed out by Iezzi et
573 al. (2018) as a possible cause for the scatter observed in scaling relationships (see e.g.,
574 Leonard, 2010; Manighetti et al., 2007; Stirling et al., 2002; Wells & Coppersmith, 1994;
575 Wesnousky, 2008), since these databases may contain information on displacement along
576 bends as well as along straight faults. Thus, if the variations in displacement rates are not
577 recognized, this can lead not only to a misinterpretation of the strain-rate, but also of the

maximum displacement, and consequently impact the calculation to derive typical values of earthquake magnitude from scaling relationships (Iezzi et al., 2018). Again, we note this is also relevant to coseismic offsets identified through palaeoseismology.

Overall, considering that the throw-rate can be tripled or reduced by a third along a fault depending on which of the throw values is used, we suggest care has to be taken when evaluating the seismic hazard of a fault. In particular, it has not yet been defined how to obtain an optimal database capable of characterising the uncertainties in hazard calculations relating to throw variations with fault geometry, and the results from one fault cannot be used to quantify this, as all faults are different in geometry. The need to use detailed measurements and understand the implications for uncertainty when using lower resolution data for seismic hazard calculations needs to be considered for hazard and risk mapping and in turn for local building planning and regulations. This is particularly relevant when planning sites suitable for critical infrastructure, for which local seismic hazard variations should be taken into consideration. It is not an aim of this article to determine a characteristic recurrence interval for the Auletta fault, however, we observed a variation of ~3.5x in strain-rate when using only one measurement of throw for our calculations, and this can lead to an overestimation or underestimation of the strain-rate, depending on which of the throw measurement is used. This translates to an equivalent change in calculated moment release in earthquakes if using degraded data (see supplementary material, Section 1). Therefore, as demonstrated by Faure Walker et al. (2018), simplified throw profiles can alter recurrence intervals and fault geometry can affect PGA and ground shaking intensities beyond uncertainties in modelled natural variability (CV). Furthermore, it has also been demonstrated that detailed fault geometry and slip measurements affects fault interaction through changing Coulomb stress calculations, which can advance or delay earthquake occurrence (Mildon et al., 2016b, 2017,

2019). Therefore, we advocate using detailed fault traces and slip-rate data in seismic hazard calculations.

6. Conclusions

In this paper, we present a detailed mapping of fault strike, dip, slip vector and throw for a well-exposed normal fault in the Southern Apennines, in order to determine the uncertainty relating to the use of those parameters in the calculations of the strain-rate across a fault. We show how fault throw and slip vector vary along the fault due to its geometry, and investigate the effect of these changes on the strain-rate. Our results show variations in throw that are detectable at a local scale (<200 m), and these are due to changes in strike and dip of the fault. We find that local anomalies in throw can affect strain-rate calculations, to the point that using only one value of throw averaged across the whole fault can produce a factor of ~3.5x difference in strain-rate. Using the short fault segment studied as an analogy for a longer fault, we suggest that measurements of slip-rates need to be taken approximately every 2 km to accurately capture the variation in throw along a fault of about 30 km so that the strain-rate and hence moment release rate across that fault can be calculated and used in seismic hazard assessment. However, we suggest that where this detail is not available, the use of fewer data can be considered acceptable when a larger scale is used to evaluate the strain-rate across a fault, but this implies a higher uncertainty that must be considered within PSHA calculations.

Acknowledgments

This work was supported by a Natural Environment Research Council studentship (grant number NE/L002485/1) to Claudia Sgambato. We thank Jennifer Robertson for assistance during fieldwork and Francesco Iezzi for discussions concerning this study. We thank Bruno Pace and three anonymous reviewers for helping to improve the manuscript.

References

Allmendinger, R. W., Cardozo, N., and Fisher, D., 2012. Structural geology algorithms: Vectors and tensors in structural geology: Cambridge University Press.

Allen, J.R., Brandt, U., Brauer, A., Hubberten, H.W., Huntley, B., Keller, J., Kraml, M., Mackensen, A., Mingram, J., Negendank, J.F. and Nowaczyk, N.R., 1999. Rapid environmental changes in southern Europe during the last glacial period. *Nature*, *400*(6746), p.740.

Amicucci, L., Barchi, M.R., Montone, P. and Rubiliani, N., 2008. The Vallo di Diano and Auletta extensional basins in the southern Apennines (Italy): a simple model for a complex setting. Terra Nova, 20(6), pp.475-482.

Anderson, H., Jackson, J., 1987. Active tectonics of the Adriatic region. Geophysical Journal of the Royal Astronomical Society 91, 937–983.

Ascione, A., Cinque, A., Tozzi, M., 1992. La valle del Tanagro (Campania): una depressione strutturale ad evoluzione complessa. Studi Geologici Camerti Spec. Vol. 1992/1, 209–219.

647 Barchi, M., Amato, A., Cippitelli, G., Merlini, S. and Montone, P., 2007. Extensional
648 tectonics and seismicity in the axial zone of the Southern Apennines. Boll. Soc. Geol.
649 It.(Italian Journal of Geosciences).

650 Benedetti L., Tapponnier P., King G.C.P., and Piccardi L., 1998. Surface Rupture of the 1857
651 Southern Italian Earthquake? Terra Nova, 10, 206-210.

652 Beck, J., Wolfers, S. and Roberts, G.P., 2018. Bayesian earthquake dating and seismic hazard
653 assessment using chlorine-36 measurements (BED v1).

654 Bernard, P. and Zollo, A., 1989. The Irpinia (Italy) 1980 earthquake: detailed analysis of a
655 complex normal faulting. Journal of Geophysical Research: Solid Earth, 94(B2),
656 pp.1631-1647.

657 Bruno, P.P., Castiello, A., Villani, F. and Improta, L., 2013. High□Resolution Densely
658 Spaced Wide□Aperture Seismic Profiling as a Tool to Aid Seismic Hazard Assessment
659 of Fault□Bounded intramontane Basins: Application to Vallo di Diano, Southern
660 Italy. Bulletin of the Seismological Society of America, 103(3), pp.1969-1980.

661 Bruno, P.P., Improta, L., Castiello, A., Villani, F. and Montone, P., 2010. The Vallo di Diano
662 Fault System: new evidence for an active range-bounding fault in southern Italy using
663 shallow, high-resolution seismic profiling. Bulletin of the Seismological Society of
664 America, 100(2), pp.882-890.

665 Bubeck, A., Wilkinson, M., Roberts, G.P., Cowie, P.A., McCaffrey, K.J.W., Phillips, R. and
666 Sammonds, P., 2015. The tectonic geomorphology of bedrock scarps on active normal
667 faults in the Italian Apennines mapped using combined ground penetrating radar and
668 terrestrial laser scanning. Geomorphology, 237, pp.38-51.

669 Cardozo, N., and Allmendinger, R.W., 2013. Spherical projections with OSXStereonet:
670 Computers & Geosciences, v. 51, p. 193 – 205, doi:10.1016/j.cageo.2012.07.021.

671 Cartwright, J.A., Trudgill, B.D. and Mansfield, C.S., 1995. Fault growth by segment linkage:
672 an explanation for scatter in maximum displacement and trace length data from the
673 Canyonlands Grabens of SE Utah. *Journal of Structural Geology*, *17*(9), pp.1319-1326.

674 Castelli V., Galli P., Camassi R., and Caracciolo C., 2008. The 1561 Earthquake(s) in
675 Southern Italy: New Insights into a Complex Seismic Sequence, Journal of Earthquake
676 Engineering, 12, 1054-1077.

677 Cavinato, G.P. and Celles, P.D., 1999. Extensional basins in the tectonically bimodal central
678 Apennines fold-thrust belt, Italy: response to corner flow above a subducting slab in
679 retrograde motion. *Geology*, *27*(10), pp.955-958.

680 Childs, C., Watterson, J. and Walsh, J.J., 1995. Fault overlap zones within developing normal
681 fault systems. *Journal of the Geological Society*, *152*(3), pp.535-549.

682 Cinque, A., Ascione, A. and Caiazzo, C., 2000. Distribuzione spazio-temporale e
683 caratterizzazione della fagliazione quaternaria in Appennino meridionale. *Le Ricerche*
684 *del GNDT nel Campo della Pericolosità Sismica: Rome, Consiglio Nazionale delle*
685 *Ricerche, Gruppo Nazionale per la Difesa dai Terremoti*, pp.203-218.

686 Cinti, F.R., Cucci, L., Pantosti, D., D'Addezio, G. and Meghraoui, M., 1997. A major
687 seismogenic fault in a 'silent area': The Castrovillari fault (southern Apennines,
688 Italy). *Geophysical Journal International*, *130*(3), pp.595-605.

689 Cowie, P.A., Phillips, R.J., Roberts, G.P., McCaffrey, K., Zijerveld, L.J.J., Gregory, L.C.,
690 Walker, J.F., Wedmore, L.N.J., Dunai, T.J., Binnie, S.A. and Freeman, S.P.H.T., 2017.

691 Orogen-scale uplift in the central Italian Apennines drives episodic behaviour of
692 earthquake faults. *Scientific reports*, *7*, p.44858.

693 Cowie, P.A. and Roberts, G.P., 2001. Constraining slip rates and spacings for active normal
694 faults. *Journal of Structural Geology*, *23*(12), pp.1901-1915.

695 Cowie, P.A., Roberts, G.P., Bull, J.M. and Visini, F., 2012. Relationships between fault
696 geometry, slip rate variability and earthquake recurrence in extensional
697 settings. *Geophysical Journal International*, *189*(1), pp.143-160.

698 Cowie, P.A., Scholz, C.H., Roberts, G.P., Walker, J.F. and Steer, P., 2013. Viscous roots of
699 active seismogenic faults revealed by geologic slip-rate variations. *Nature*
700 *Geoscience*, *6*(12), p.1036.

701 D'Agostino, N., S. Mantenuto, E. D'Anastasio, R. Giuliani, M. Mattone, S. Calcaterra, P.
702 Gambino, and L. Bonci, 2011. Evidence for localized active extension in the central
703 Apennines (Italy) from global positioning system observations, Geology, 39(4), 291–
704 294, doi:10.1130/G31796.1.

705 Doglioni, C., 1993. Some remarks on the origin of foredeeps. Tectonophysics 228, 1–20.

706 Ellis, M.A. and Dunlap, W.J., 1988. Displacement variation along thrust faults: Implications
707 for the development of large faults. *Journal of Structural Geology*, *10*(2), pp.183-192.

708 Ellsworth, W.L., Matthews, M.V., Nadeau, R.M., Nishenko, S.P., Reasenberg, P.A. and
709 Simpson, R.W., 1999. A physically-based earthquake recurrence model for estimation
710 of long-term earthquake probabilities. *US Geol. Surv. Open-File Rept. 99*, *522*, p.23.

711 Faure Walker, J. P., 2010. Mechanics of continental extension from Quaternary strain field in
712 the Italian Apennines. Ph.D. thesis, University College London.

713 Faure Walker, J. P., Roberts, G. P., Cowie, P. A., Papanikolaou, I. D., Sammonds, P. R.,
714 Michetti, A. M., & Phillips, R. J., 2009. Horizontal strain-rates and throw-rates across
715 breached relay zones, Central Italy: Implications for the preservation of throw deficits
716 at points of normal fault linkage. Journal of Structural Geology, 31(10), 1145–1160.
717 https://doi.org/10.1016/j.jsg.2009.06.011

718 Faure Walker, J. P., Roberts, G. P., Sammonds, P. R., & Cowie, P. A., 2010. Comparison of
719 earthquake strains over 10 2 and 10 4 year timescales: Insights into variability in the
720 seismic cycle in the central Apennines, Italy. Journal of Geophysical Research, 115,
721 B10418. https://doi.org/10.1029/2009JB006462.

722 Faure Walker, J. P., G. P. Roberts, P. A. Cowie, I. Papanikolaou, A. M. Michetti, P.
723 Sammonds, M. Wilkinson, K. J. W. McCaffrey, and R. J. Phillips, 2012. Relationship
724 between topography, rates of extension and mantle dynamics in the actively-extending
725 Italian Apennines, Earth Planet. Sci. Lett., 325-326, 76–84,
726 doi:10.1016/j.epsl.2012.01.028.

727 Faure Walker J.P., G. P. Roberts, P. A. Cowie, K. McCaffrey. L. Wedmore, Z. Watson, L. C.
728 Gregory, 2015. Long-term strain rates as a tool for understanding the mechanics of
729 continental extension and the importance of local 3D fault geometry for local throw-
730 rates across faults. 6th Int. INQUA meeting on Paleoseismology, active tectonics and
731 Archaeoseismology, 19-24 April 2015, Pescina, Fucino Basin, Italy, 27,150–154.

732 Faure Walker, J.P., Visini, F., Roberts, G., Galasso, C., McCaffrey, K. and Mildon, Z., 2018.
733 Variable Fault Geometry Suggests Detailed Fault□Slip□Rate Profiles and Geometries

734 Are Needed for Fault□Based Probabilistic Seismic Hazard Assessment
735 (PSHA). *Bulletin of the Seismological Society of America*, *109*(1), pp.110-123.

736 Field, E.H., Arrowsmith, R.J., Biasi, G.P., Bird, P., Dawson, T.E., Felzer, K.R., Jackson,
737 D.D., Johnson, K.M., Jordan, T.H., Madden, C. and Michael, A.J., 2014. Uniform
738 California earthquake rupture forecast, version 3 (UCERF3)—The time□independent
739 model. *Bulletin of the Seismological Society of America*, *104*(3), pp.1122-1180.

740 Foxford, K.A., Walsh, J.J., Watterson, J., Garden, I.R., Guscott, S.C. and Burley, S.D., 1998.
741 Structure and content of the Moab Fault Zone, Utah, USA, and its implications for fault
742 seal prediction. *Geological Society, London, Special Publications*, *147*(1), pp.87-103.

743 Galadini, F. and Galli, P., 1999. The Holocene paleoearthquakes on the 1915 Avezzano
744 earthquake faults (central Italy): implications for active tectonics in the central
745 Apennines. *Tectonophysics*, *308*(1-2), pp.143-170.

746 Galadini, F., Galli, P. and Giraudi, C., 1997. Geological investigations of Italian earthquakes:
747 new paleoseismological data from the Fucino Plain (Central Italy). *Journal of*
748 *Geodynamics*, *24*(1-4), pp.87-103.

749 Galli, P. and Galadini, F., 2003. Disruptive earthquakes revealed by faulted archaeological
750 relics in Samnium (Molise, southern Italy). *Geophysical Research Letters*, *30*(5).

751 Galli, P., Galadini, F. and Calzoni, F., 2005. Surface faulting in Norcia (central Italy): a
752 “paleoseismological perspective”. *Tectonophysics*, *403*(1-4), pp.117-130.

753 Galli, P., Bosi, V., Piscitelli, S., Giocoli, A. and Scionti, V., 2006. Late Holocene earthquakes
754 in southern Apennine: paleoseismology of the Caggiano fault. International Journal of
755 Earth Sciences, 95(5), pp.855-870.

Galli, P., Galadini, F. and Pantosti, D., 2008. 'Twenty years of paleoseismology in Italy', Earth-Science Reviews, 88(1–2), pp. 89–117. doi: 10.1016/j.earscirev.2008.01.001.

Giraudi, C., 1995. I detriti di versante al margine della piana del Fucino (Italia centrale): significato palaeoclimatico ed impatto antropico. Il Quaternario 8, 203–210.

Giraudi, C. and Frezzotti, M., 1997. Late Pleistocene glacial events in the central Apennines, Italy. *Quaternary Research*, *48*(3), pp.280-290.

Gioia, D.A.R.I.O., Di Leo, P.A.O.L.A., Mattei, M.A.S.S.I.M.O., Schiattarella, M.A.R.C.E.L.L.O., Zucali, M.I.C.H.E.L.E., Chateigner, D.A.N.I.E.L. and Ouladdiaf, B.A.C.H.I.R., 2010. Opening kinematics of the Auletta and Vallo di Diano basins, southern Italy: constraints from structural analysis, paleomagnetism, and neutron texture analysis. Rendiconti online della Società Geologica Italiana, 10, pp.61-64.

González, Á., Gómez, J.B. and Pacheco, A.F., 2006. Updating seismic hazard at Parkfield. *Journal of seismology*, *10*(2), pp.131-135.

E. Guidoboni, G. Ferrari, D. Mariotti, A. Comastri, G. Tarabusi, G. Sgattoni, G. Valensise, 2018. CFTI5Med, Catalogo dei Forti Terremoti in Italia (461 a.C.-1997) e nell'area Mediterranea (760 a.C.-1500). Istituto Nazionale di Geofisica e Vulcanologia (INGV). doi: https://doi.org/10.6092/ingv.it-cfti5.

Gupta, A. and Scholz, C.H., 2000. A model of normal fault interaction based on observations and theory. *Journal of Structural Geology*, *22*(7), pp.865-879.

Hippolyte, J.C., Angelier, J. and Roure, F.B., 1994. A major geodynamic change revealed by Quaternary stress patterns in the Southern Apennines (Italy). Tectonophysics, 230(3-4), pp.199-210.

778 Iezzi, F., Mildon, Z., Walker, J. F., Roberts,G., Goodall, H., Wilkinson, M., & Robertson, J.,
779 2018. Coseismic throw variation across along-strike bends on active normal faults:
780 Implications for displacement versus length scaling of earthquake ruptures. Journal of
781 Geophysical Research: Solid Earth, 123. https://doi.org/10.1029/2018JB016732.

782 Iezzi, F., Roberts, G., Walker, J.F. and Papanikolaou, I., 2019. Occurrence of partial and total
783 coseismic ruptures of segmented normal fault systems: Insights from the Central
784 Apennines, Italy. *Journal of Structural Geology*.

785 Kendrick, K.J., Morton, D.M., Wells, S.G. and Simpson, R.W., 2002. Spatial and temporal
786 deformation along the northern San Jacinto fault, southern California: Implications for
787 slip rates. *Bulletin of the Seismological Society of America*, *92*(7), pp.2782-2802.

788 Kostrov, V.V., 1974. Seismic moment and energy of earthquakes, and seismic flow of rock.
789 Izv. Earth Physics 1 (23–40), 13–21. translation UDC 550.341.

790 Leonard, M., 2010. Earthquake fault scaling: Self-consistent relating of rupture length, width,
791 average displacement, and moment release. *Bulletin of the Seismological Society of*
792 *America*, *100*(5A), pp.1971-1988.

793 Lienkaemper, J.J. and Williams, P.L., 2007. A record of large earthquakes on the southern
794 Hayward fault for the past 1800 years. *Bulletin of the Seismological Society of*
795 *America*, *97*(6), pp.1803-1819.

796 Ma, X.Q. and Kusznir, N.J., 1995. Coseismic and postseismic subsurface displacements and
797 strains for a dip□slip normal fault in a three□layer elastic□gravitational
798 medium. *Journal of Geophysical Research: Solid Earth*, *100*(B7), pp.12813-12828.

799 Manighetti, I., Campillo, M., Bouley, S. and Cotton, F., 2007. Earthquake scaling, fault
800 segmentation, and structural maturity. *Earth and Planetary Science Letters*, *253*(3-4),
801 pp.429-438.

802 Maschio, L., Ferranti, L. and Burrato, P., 2005. Active extension in Val d'Agri area, Southern
803 Apennines, Italy: implications for the geometry of the seismogenic belt. *Geophysical*
804 *Journal International*, *162*(2), pp.591-609.

805 McLeod, A.E., Dawers*, N.H. and Underhill, J.R., 2000. The propagation and linkage of
806 normal faults: insights from the Strathspey–Brent–Statfjord fault array, northern North
807 Sea. *Basin Research*, *12*(3□4), pp.263-284.

808 Mildon, Z.K., Roberts, G.P., Walker, J.P.F., Wedmore, L.N. and McCaffrey, K.J., 2016a.
809 Active normal faulting during the 1997 seismic sequence in Colfiorito, Umbria: Did
810 slip propagate to the surface?. Journal of Structural Geology, 91, pp.102-113.

811 Mildon, Z.K., Toda, S., Faure Walker, J.P. and Roberts, G.P., 2016b. Evaluating models of
812 Coulomb stress transfer: Is variable fault geometry important?. Geophysical Research
813 Letters, 43(24).

814 Mildon, Z.K., Roberts, G.P., Faure Walker, J.P. and Iezzi, F., 2017. Coulomb stress transfer
815 and fault interaction over millennia on non-planar active normal faults: the M w 6.5–
816 5.0 seismic sequence of 2016–2017, central Italy. *Geophysical Journal*
817 *International*, *210*(2), pp.1206-1218.

818 Mildon, Z., Roberts, G., Walker, J.F. and Toda, S., 2018. Coulomb pre-stress and fault bends:
819 ignored yet vital factors for earthquake triggering.

820 Michetti, A.M., Brunamonte, F., Serva, L., Vittori, E., 1996. Trench investigations of the
821 1915 Fucino earthquake fault scarps (Abruzzo, Central Italy): geological evidence of
822 large historical events. Journal of Geophysical Research 101, 5921–5936.

823 Maschio, L., Ferranti, L. and Burrato, P., 2005. Active extension in Val d'Agri area, Southern
824 Apennines, Italy: implications for the geometry of the seismogenic belt. Geophysical
825 Journal International, 162(2), pp.591-609.

826 Moro, M., Amicucci, L., Cinti, F.R., Doumaz, F., Montone, P., Pierdominici, S., Saroli, M.,
827 Stramondo, S. and Di Fiore, B., 2007. Surface evidence of active tectonics along the
828 Pergola-Melandro fault: a critical issue for the seismogenic potential of the southern
829 Apennines, Italy. J. Geodyn. Doi: 10.1016/j.jog.2006.12.003.

830 Mostardini, F., Merlini, S., 1986. Appennino centro meridionale, sezioni geologiche e
831 proposta di modello strutturale. Memorie della Societa Geologica Italiana 35, 177-202.

832 Pace, B., Peruzza, L., Lavecchia, G. and Boncio, P., 2006. Layered seismogenic source
833 model and probabilistic seismic-hazard analyses in central Italy. *Bulletin of the*
834 *Seismological Society of America*, *96*(1), pp.107-132.

835 Pace, B., Bocchini, G. M. and Boncio, P., 2014. 'Do static stress changes of a moderate-
836 magnitude earthquake significantly modify the regional seismic hazard? Hints from the
837 L'Aquila 2009 normal-faulting earthquake (Mw 6.3, central Italy)', Terra Nova, 26(6),
838 pp. 430–439. doi: 10.1111/ter.12117.

839 Patacca, E., Sartori, R., Scandone, P., 1990. Tyrrhenian Basin and Apenninic Arcs: kinematic
840 relations since late Tortonian times. Mem. Soc. Geol. It. 45, 425–451.

841 Papanikolaou, I.D., Roberts, G.P., 2007. Geometry, kinematics and deformation rates along
842 the active normal fault system in the southern Apennines: implications for fault growth.
843 J. Struct. Geol. 29, 166–188.

844 Palumbo, L., L. Benedetti, D. Bourlès, A. Cinque, and R. Finkel, 2004. Slip history of the
845 Magnola fault (Apennines, Central Italy) from 36Cl surface exposure dating: Evidence
846 for strong earthquakes over the Holocene, Earth Planet. Sci. Lett., 225(1-2), 163–176,
847 doi:10.1016/j. epsl.2004.06.012.

848 Pantosti, D., D'Addezio, G. and Cinti, F.R., 1993. Paleoseismological evidence of repeated
849 large earthquakes along the 1980 Irpinia earthquake fault.

850 Pantosti, D., D'Addezio, G., Cinti, F., 1996. Paleoseismicity of the Ovindoli–Pezza fault,
851 central Apennines, Italy: a history including a large, previously unrecorded earthquake
852 in the Middle Ages (860–1300 A.D.). Journal of Geophysical Research 101, 5937–
853 5960.

854 Pantosti, D. and Valensise, G., 1990. Faulting mechanism and complexity of the November
855 23, 1980, Campania□Lucania earthquake, inferred from surface observations. *Journal*
856 *of Geophysical Research: Solid Earth*, *95*(B10), pp.15319-15341.

857 Peacock, D.C.P. and Sanderson, D.J., 1994. Geometry and development of relay ramps in
858 normal fault systems. *AAPG bulletin*, *78*(2), pp.147-165.

859 Peruzza, L., Pace, B. and Visini, F., 2011. Fault-based earthquake rupture forecast in Central
860 Italy: remarks after the L'Aquila Mw 6.3 event. Bull. Seismol. Soc. Am., 101, 404–
861 412.

862 Roberts, G.P., Michetti, A.M., 2004. Spatial and temporal variations in growth rates along
863 active normal fault Systems: an example from Lazio-Abruzzo, central Italy. Journal of
864 Structural Geology 26, 339e376.

865 Roberts G.P., 1996. Variation in fault slip directions along active and segmented normal fault
866 systems, Journal of Structural Geology, 18, 835-845.

867 Roberts G.P., 2007. Fault orientation variations along the strike of active normal fault
868 systems in Italy and Greece: Implications for predicting the orientations of subseismic-
869 resolution faults in hydrocarbon reservoirs, AAPG Bulletin, 91 (1), 1-20.

870 Roberts, G.P., 2008. Visualisation of active normal fault scarps in the Apennines, Italy: a key
871 to assessment of tectonic strain release and earthquake rupture. *Journal of the Virtual*
872 *Explorer*, *29*.

873 Rovida A., Locati M., Camassi R., Lolli B., Gasperini P. (eds), 2016. CPTI15, the 2015
874 version of the Parametric Catalogue of Italian Earthquakes. Istituto Nazionale di
875 Geofisica e Vulcanologia. doi:http://doi.org/10.6092/INGV.IT-CPTI15.

876 Schlagenhauf A, Gaudemer Y, Benedetti L, Manighetti I, Palumbo L, Schimmelpfennig I,
877 Finkel R, Pou K., 2010. Using in situ Chlorine-36 cosmonuclide to recover past
878 earthquake histories on limestone normal fault scarps: a reappraisal of methodology
879 and interpretations. Geophysical Journal International 182: 36-72
880 http://dx.doi.org/10.1111/j.1365-246X.2010.04622.x.

881 Schlagenhauf, A., Manighetti, I., Benedetti, L., Gaudemer, Y., Finkel, R., Malavieille, J. and
882 Pou, K., 2011. Earthquake supercycles in Central Italy, inferred from 36Cl exposure
883 dating. Earth and Planetary Science Letters, 307(3-4), pp.487-500.

884 Shen, Z.K., Sun, J., Zhang, P., Wan, Y., Wang, M., Bürgmann, R., Zeng, Y., Gan, W., Liao,
885 H. and Wang, Q., 2009. Slip maxima at fault junctions and rupturing of barriers during
886 the 2008 Wenchuan earthquake. *Nature geoscience*, *2*(10), p.718.

887 Soliva, R., Benedicto, A., Schultz, R.A., Maerten, L. and Micarelli, L., 2008. Displacement
888 and interaction of normal fault segments branched at depth: Implications for fault
889 growth and potential earthquake rupture size. Journal of Structural Geology, 30(10),
890 pp.1288-1299.

891 Spina, V., Tondi, E., Galli, P., Mazzoli, S. and Cello, G., 2008. Quaternary fault
892 segmentation and interaction in the epicentral area of the 1561 earthquake (Mw= 6.4),
893 Vallo di Diano, southern Apennines, Italy. Tectonophysics, 453(1-4), pp.233-245.

894 Stirling, M., Rhoades, D. and Berryman, K., 2002. Comparison of earthquake scaling
895 relations derived from data of the instrumental and preinstrumental era. *Bulletin of the*
896 *Seismological Society of America*, *92*(2), pp.812-830.

897 Tarquini S., Isola I., Favalli M., Mazzarini F., Bisson M., Pareschi M. T., Boschi E., 2007.
898 TINITALY/01: a new Triangular Irregular Network of Italy, Annals of Geophysics 50,
899 407 - 425.

900 Tarquini S., Vinci S., Favalli M., Doumaz F., Fornaciai A., Nannipieri L., 2012. Release of a
901 10-m-resolution DEM for the Italian territory: Comparison with global-coverage DEMs
902 and anaglyph-mode exploration via the web, Computers & Geosciences 38, 168-170.
903 doi: doi:10.1016/j.cageo.2011.04.018

904 Tarquini S., Nannipieri L., 2017. The 10 m-resolution TINITALY DEM as a trans-
905 disciplinary basis for the analysis of the italian territory: Current trends and new
906 perspectives, Geomorphology doi: 10.1016/j.geomprph.2016.12.022

907 Taylor, S.K., Bull, J.M., Lamarche, G. and Barnes, P.M., 2004. Normal fault growth and
908 linkage in the Whakatane Graben, New Zealand, during the last 1.3 Myr. *Journal of*
909 *Geophysical Research: Solid Earth*, *109*(B2).

910 Tesson, J. and Benedetti, L., 2019. Seismic history from in situ 36Cl cosmogenic nuclide data
911 on limestone fault scarps using Bayesian reversible jump Markov chain Monte
912 Carlo. *Quaternary Geochronology*.

913 Tesson, J., Pace, B., Benedetti, L., Visini, F., Delli Rocioli, M., Arnold, M., Aumaître, G.,
914 Bourlès, D.L. and Keddadouche, K., 2016. Seismic slip history of the Pizzalto fault
915 (central Apennines, Italy) using in situ□produced 36Cl cosmic ray exposure dating and
916 rare earth element concentrations. *Journal of Geophysical Research: Solid*
917 *Earth*, *121*(3), pp.1983-2003.

918 Tucker, G.E., McCoy, S.W., Whittaker, A.C., Roberts, G.P., Lancaster, S.T. and Phillips, R.,
919 2011. Geomorphic significance of postglacial bedrock scarps on normal□fault
920 footwalls. *Journal of Geophysical Research: Earth Surface*, *116*(F1).

921 Valensise G. and Pantosti D., 2001. The investigation of potential earthquake sources
922 peninsular Italy: A review, Journal of Seismology, 5 (3), 287-306.

923 Valentini, A., F. Visini, and B. Pace, 2017. Integrating faults and past earthquakes into a
924 probabilistic seismic hazard model for peninsular Italy, Nat. Hazards Earth Sci. Syst.
925 Sci. 17, no. 11, doi: 10.5194/nhess-17-2017-2017.

926 Villani, F. and Pierdominici, S., 2010. Late Quaternary tectonics of the Vallo di Diano basin
927 (southern Apennines, Italy). Quaternary Science Reviews, 29(23-24), pp.3167-3183.

928 Visini, F. and Pace, B., 2014. Insights on a key parameter of earthquake forecasting, the
929 coefficient of variation of the recurrence time, using a simple earthquake
930 simulator. Seismological Research Letters, 85(3), pp.703-713.

931 Wesnousky, S.G., 2008. Displacement and geometrical characteristics of earthquake surface
932 ruptures: Issues and implications for seismic-hazard analysis and the process of
933 earthquake rupture. *Bulletin of the Seismological Society of America*, *98*(4), pp.1609-
934 1632.

935 Westaway, R. and Jackson, J., 1987. The earthquake of 1980 November 23 in Campania—
936 Basilicata (southern Italy). *Geophysical Journal International*, *90*(2), pp.375-443.

937 Wilkinson M., Roberts G.P., McCaffrey K., Cowie P. A., Faure Walker J.P., Papanikolaou I.,
938 Phillips J.R., Michetti A.M., Vittori E., Gregory L., Wedmore L., Watson Z.K., 2015.
939 Slip distributions on active normal faults measured from LiDAR and field mapping of
940 geomorphic offsets: an example from L'Aquila, Italy, and implications for modelling
941 seismic moment release, Geomorphology, Volume 237, 2015, Pages 130-141,
942 https://doi.org/10.1016/j.geomorph.2014.04.026.

943 Working Group on Utah Earthquake Probabilities (WGUEP), 2016. Earthquake probabilities
944 for the Wasatch Front region in Utah, Idaho, and Wyoming: Utah Geological Survey
945 Miscellaneous Publication 16-3, 164 p., 5 appendices.

946 Wu, D. and Bruhn, R.L., 1994. Geometry and kinematics of active normal faults, South
947 Oquirrh Mountains, Utah: implication for fault growth. *Journal of Structural*
948 *Geology*, *16*(8), pp.1061-1075.

949

950 **Figures captions**

951

952 Figure 1. The figure shows a location map of the studied area. (a) Red lines are active faults
953 of the Italian Central and Southern Apennines (based on map in Faure Walker et al., 2012),
954 the black box represents the area covered by (b). (b) More detailed map of the studied area, in
955 UTM coordinates. Active faults are shown as black lines with tick marks on the hangingwall;
956 the studied fault, called the Auletta fault, is shown in the blue box; a detailed map of the
957 studied fault is shown in Figure 2. The black arrows indicate the slip vector direction, adapted
958 from Papanikolaou & Roberts (2007). Historical earthquakes with Mw≥5.5 are indicated on
959 the map, with colour coding indicating the epicentral intensity (Mercalli-Cancani-Sieberg
960 scale) from CFTI5Med (Guidoboni et al., 2018). Figure created using 10 m resolution Digital
961 Elevation Models (Tarquini et al., 2007, 2012, 2017).

962

963 Figure 2. Structural map of the studied fault. (a) Location map of the area covered by (b) and
964 (c). (b) Structural map of the Auletta fault; data collected along the fault length A-B are
965 shown in Figure 3. Black line represents the trace of the fault scarp, formed in the last 15±3
966 kyr. Black arrows represent the direction of the mean slip vector, with azimuth and plunge,
967 calculated within 8 sections of the fault, based on geometrical variations; average values
968 calculated within those sections are shown in Figure 4. Mean strike and dip are shown in
969 white. Blue dots represent the locations of the scarp profiles produced in this work, with site

location number in brackets; green dots are scarp profiles from previous works (Papanikolaou & Roberts, 2007; Faure Walker et al., 2012), with site location number in brackets. Stereonet for the whole dataset of the fault shows mean slip-vector azimuth and plunge (61→ 209). The yellow dashed box represents the area covered by (c). (c) Detailed geological and structural map of the south-eastern section of the Auletta fault. Black arrows indicate the mean slip-vector azimuth and plunge, measured from kinematic indicators at 15 locations, with the corresponding stereographic projections; mean value of the slip vector for the total area is shown in the large stereographic projection (61→ 211). The scarp profiles constructed for this work are represented as blue lines, with site location number in brackets and the value of throw shown in blue. The figure shows the detailed mapping carried out on the Auletta fault. The map well represents the high variability of fault geometry; throw and slip vector are influenced by such variations.

Figure 3. All field data collected and plotted against the distance A-B, as shown in Figure 2b. The figure shows that variations of throw are strongly related to changes in dip, with anomalous local increase where the dip is higher. (a) Trace of the Auletta fault. Blue dots indicate the location of the scarp profiles produced in this work; in green, locations of the scarp profiles from previous works (Papanikolaou & Roberts, 2007; Faure Walker et al., 2012). (b) Mean fault strike against distance for each data collection site. Error bars are standard errors. The grey line represents the mean strike for the whole fault, N127. (c) Mean fault dip against distance calculated at each data collection site. Error bars are standard errors. The grey line represents the mean dip for the whole fault, corresponding to 63°. (d) Mean kinematic plunge direction for each data collection site. Where it was not possible to measure in the field, the kinematic was derived from b-axis calculation in Stereonet 10.0 (Allmendinger et al., 2012; Cardozo et al., 2013). The grey line represents the mean slip

vector plunge direction for the whole fault, N209. (e) Post 15-18 kyr throw plotted against distance A-B. Error bars are ±1 m. The grey line represents the weighted average of the measurements, 4.27 m.

Figure 4. Field data collected along the total length of the Auletta fault and plotted against the distance A-B, as shown in Figure 2b. The average values are calculated within 8 sections of the fault, represented in different colours, based on variations of the fault plane. The figure shows variations of throw along the fault, with a general increase toward its Eastern tip, and highlights that local anomalies in throw are strongly related to changes in dip, with increase in throw where the dip is higher. (a) Auletta fault trace. Blue dots are locations of the scarp profiles produced in this work; in green, locations of the scarp profiles from previous works (Papanikolaou & Roberts, 2007; Faure Walker et al., 2012). The colours represent different sections of the fault, where the average values have been calculated. (b) Average fault strike against distance. Error bars are standard errors. The grey line represents the mean strike for the whole fault, N127. (c) Average fault dip against distance. Error bars are standard errors. The grey line represents the mean dip for the whole fault, 63°. Higher dip values are related to higher values of throw. (d) Average kinematic plunge direction against distance. The grey line represents the mean slip vector plunge direction for the whole fault, N209. (e) Post 15-18 ky throw plotted against distance A-B. Error bars are ±1 m. The grey line represents the weighted average of the measurements, 4.27 m.

Figure 5. Topographic profiles across the Auletta fault scarp, showing the variation of throw across the fault, with a general increasing of vertical offset towards the South-east. Locations of the profiles are indicated in Figure 2b and 2c; numbers in blue indicate the location of profiles produced in this work, in green the location of profiles from previous works (profiles

(2), (5) and (9) adapted from Papanikolaou & Roberts (2007); profiles (3) and (11) adapted from Faure Walker et al. (2012)).

Figure 6. Strain-rate calculations across the Auletta fault, using all available data and degraded datasets. The values used within the calculations are provided in Table 1. The data point on the right of the plot represents the strain-rate calculated using all the available values of throw (eleven measurements); the iterations are performed calculating the strain-rate, removing progressively one measurement from the dataset. Data points on the left end of the graph represent calculated strain-rate using a single value of throw. The grey shaded box represents the error in strain-rate, defined as ± 1σ, calculated only for the model that uses all the 11 measurements. Yellow points represent the median for the degraded points. (a) Strain-rate calculated using a grid with boxes of 200 m x 2 km. (b) Strain-rate calculated within 2 km x 2 km grid boxes. The plots show a convergence of the data towards the all data model, when more values of throw are progressively added to the calculation. The high variability of strain-rate, when this is calculated using only one value of throw is detectable at any scale.

Figure 7. Similar format to Figure 4 in Faure Walker et al. (2018). Plots show how 15kyr strain-rates in a regular 100 m x 2 km grid change along the Auletta scarp and how using degraded data for the throw profiles affects the calculated strain-rates across the fault. (a) Throw profiles along the fault for each of the models and (b) strain-rates within 100 m x 2 km grid boxes along the fault. (i) 'all data' uses all the data from the eleven data collection sites along the fault. (ii-1) 'boxcar-max' only uses the data from the maximum throw-rate site, (ii-2) 'boxcar-mean' uses the average 15ka throw, slip vector azimuth and plunge, and (ii-3) 'boxcar-min' uses only data collected from the minimum throw-rate site (above zero). In each 'boxcar' scenario, the value of throw is projected along the entire length of the

fault until near the fault tips where the throw rapidly decreases to zero. (iii-1) 'max-mid-triangle', like 'boxcar-max', only uses the data from the maximum throw-rate site, but in this scenario the throw-rate decreases linearly from the maximum at the middle of the fault to zero at each tip forming a triangular throw-rate profile along the fault; (iii-2) 'max-point-triangle' uses the maximum throw-rate value, but in this case the throw-rate decreases from the point where the maximum throw has been actually measured on the fault, to zero at the tip. Error bars and dotted bar plots shown in each plot are for the 'all data' case (i). Percentage values give the total strain-rate across the fault relative to the 'all data' case (i). This shows that degrading data by extrapolating a single throw value along a fault changes calculated strain-rates across the fault.

Tables

Table 1: field data used for the strain-rate calculations. Where 'Source' is blank, new fieldwork data are used.

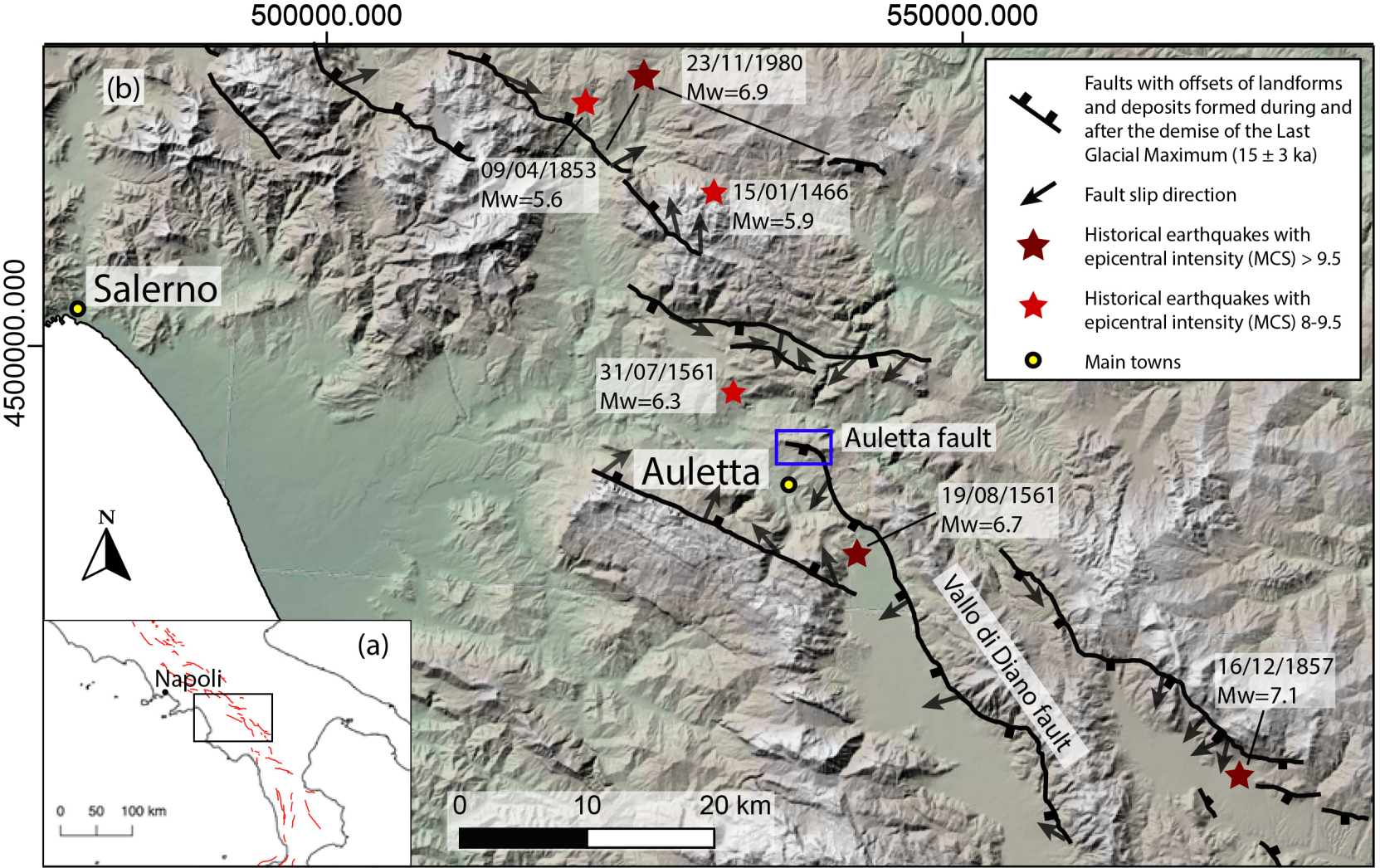
500000.000
550000.000
4500000.000
(b)
23/11/1980
Mw=6.9
09/04/1853
Mw=5.6
15/01/1466
Mw=5.9
Salerno
31/07/1561
Mw=6.3
Auletta fault
Auletta
19/08/1561
Mw=6.7
Vallo di Diano fault
16/12/1857
Mw=7.1
N
(a)
Napoli
0 50 100 km
0 10 20 km
Faults with offsets of landforms and deposits formed during and after the demise of the Last Glacial Maximum (15 ± 3 ka)
Fault slip direction
Historical earthquakes with epicentral intensity (MCS) > 9.5
Historical earthquakes with epicentral intensity (MCS) 8-9.5
Main towns

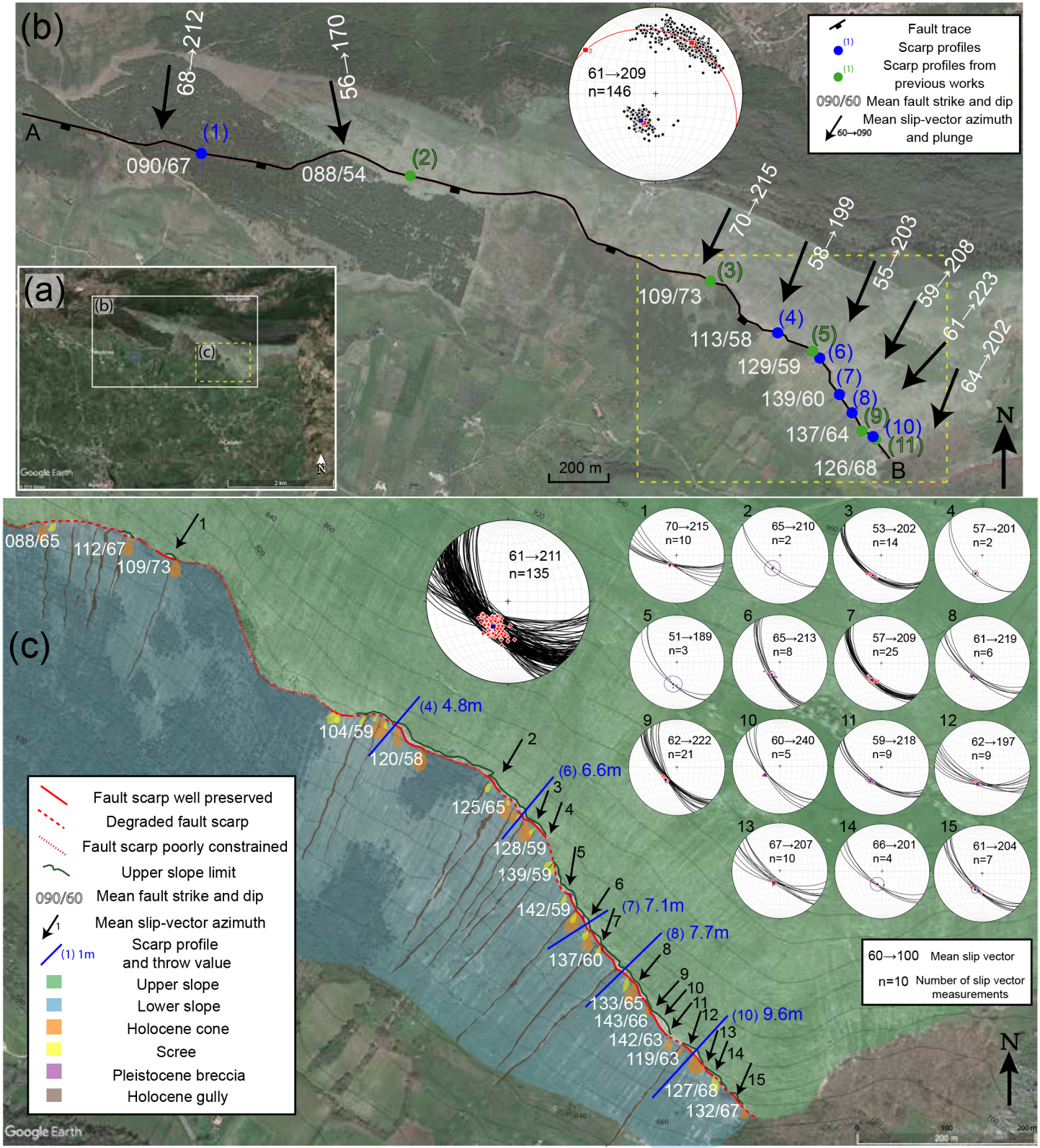
(b)
A
B
(1)
(2)
(3)
(4)
(5)
(6)
(7)
(8)
(9)
(10)
(11)
090/67
088/54
109/73
113/58
129/59
139/60
137/64
126/68
68→212
56→170
70→215
58→199
55→203
59→208
61→223
64→202
61→209
n=146
Fault trace
Scarp profiles
Scarp profiles from previous works
090/60 Mean fault strike and dip
60→090 Mean slip-vector azimuth and plunge
(a)
(b)
(c)
Google Earth
2 km
200 m
N
(c)
088/65
112/67
109/73
104/59
120/58
125/65
128/59
139/59
142/59
137/60
133/65
143/66
142/63
119/63
127/68
132/67
(4) 4.8m
(6) 6.6m
(7) 7.1m
(8) 7.7m
(10) 9.6m
61→211
n=135
1 70→215 n=10
2 65→210 n=2
3 53→202 n=14
4 57→201 n=2
5 51→189 n=3
6 65→213 n=8
7 57→209 n=25
8 61→219 n=6
9 62→222 n=21
10 60→240 n=5
11 59→218 n=9
12 62→197 n=9
13 67→207 n=10
14 66→201 n=4
15 61→204 n=7
Fault scarp well preserved
Degraded fault scarp
Fault scarp poorly constrained
Upper slope limit
090/60 Mean fault strike and dip
Mean slip-vector azimuth
(1) 1m Scarp profile and throw value
Upper slope
Lower slope
Holocene cone
Scree
Pleistocene breccia
Holocene gully
60→100 Mean slip vector
n=10 Number of slip vector measurements
Google Earth
0 100 200 m

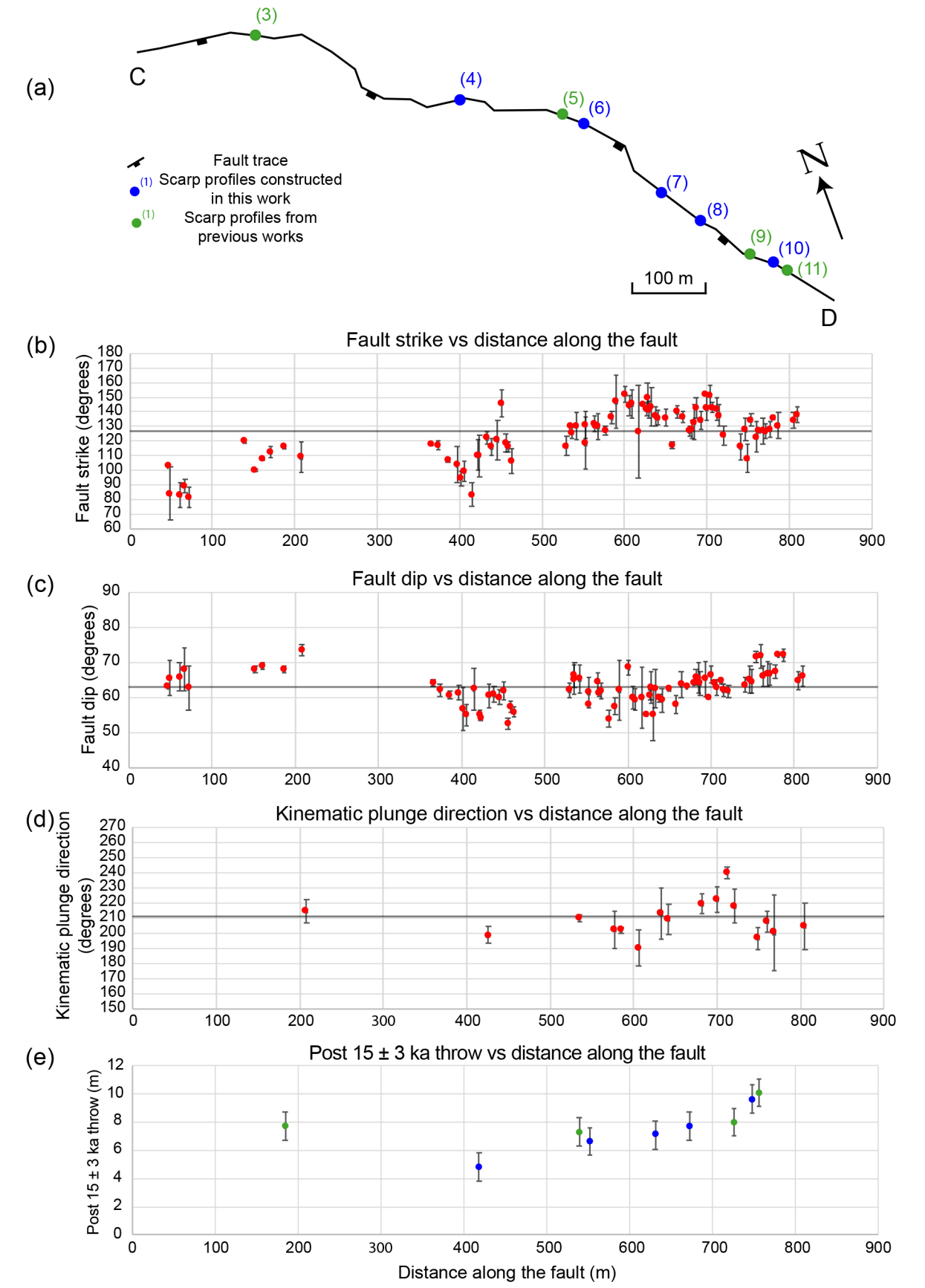
(a)
C
D
(3)
(4)
(5)
(6)
(7)
(8)
(9)
(10)
(11)
Fault trace
(1) Scarp profiles constructed in this work
(1) Scarp profiles from previous works
N
100 m
(b)
Fault strike vs distance along the fault
Fault strike (degrees)
(c)
Fault dip vs distance along the fault
Fault dip (degrees)
(d)
Kinematic plunge direction vs distance along the fault
Kinematic plunge direction (degrees)
(e)
Post 15 ± 3 ka throw vs distance along the fault
Post 15 ± 3 ka throw (m)
Distance along the fault (m)

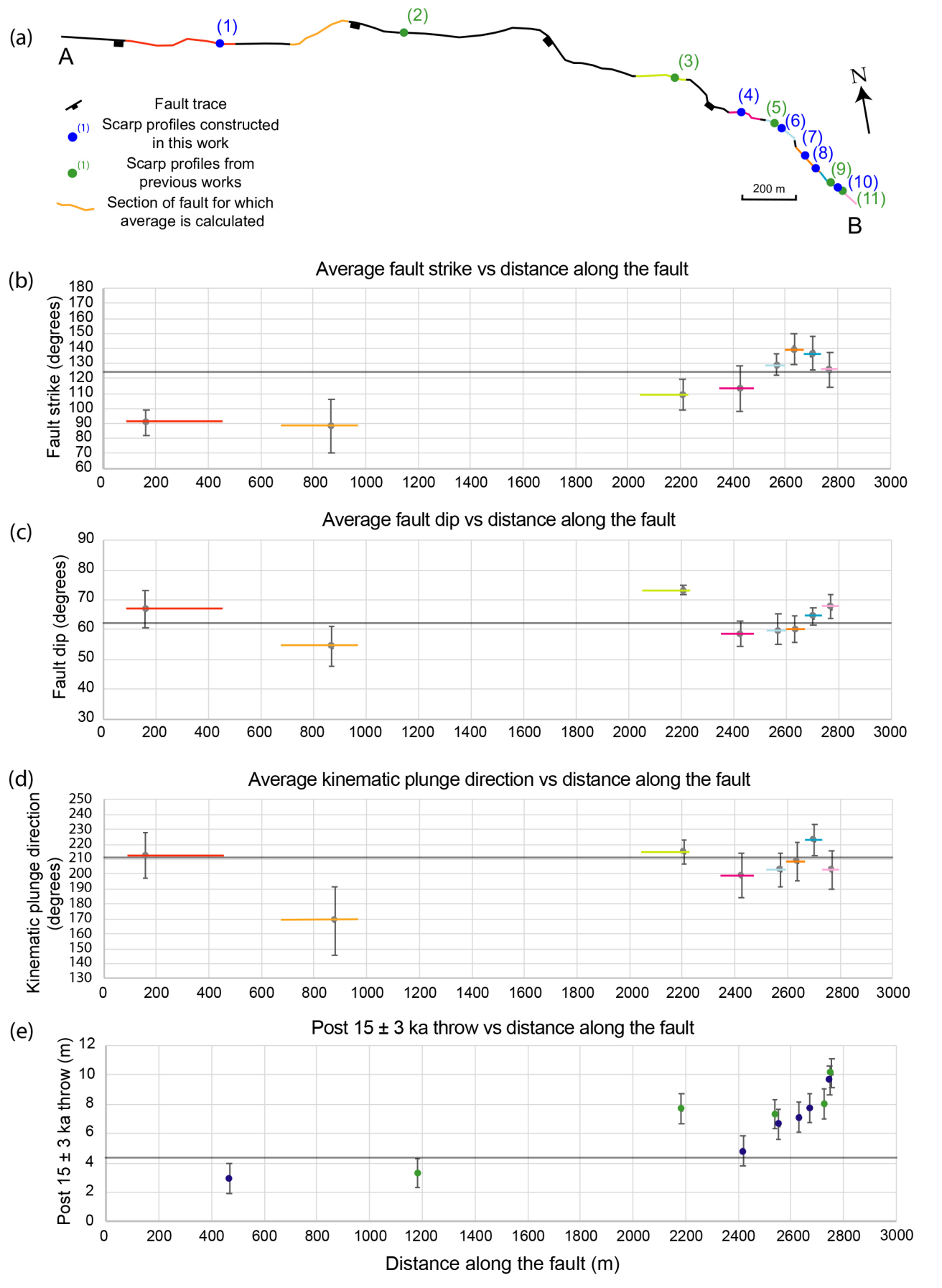
(a)
A
B
(1)
(2)
(3)
(4)
(5)
(6)
(7)
(8)
(9)
(10)
(11)
N
200 m
Fault trace
Scarp profiles constructed in this work
Scarp profiles from previous works
Section of fault for which average is calculated
(b)
Average fault strike vs distance along the fault
Fault strike (degrees)
(c)
Average fault dip vs distance along the fault
Fault dip (degrees)
(d)
Average kinematic plunge direction vs distance along the fault
Kinematic plunge direction (degrees)
(e)
Post 15 ± 3 ka throw vs distance along the fault
Post 15 ± 3 ka throw (m)
Distance along the fault (m)

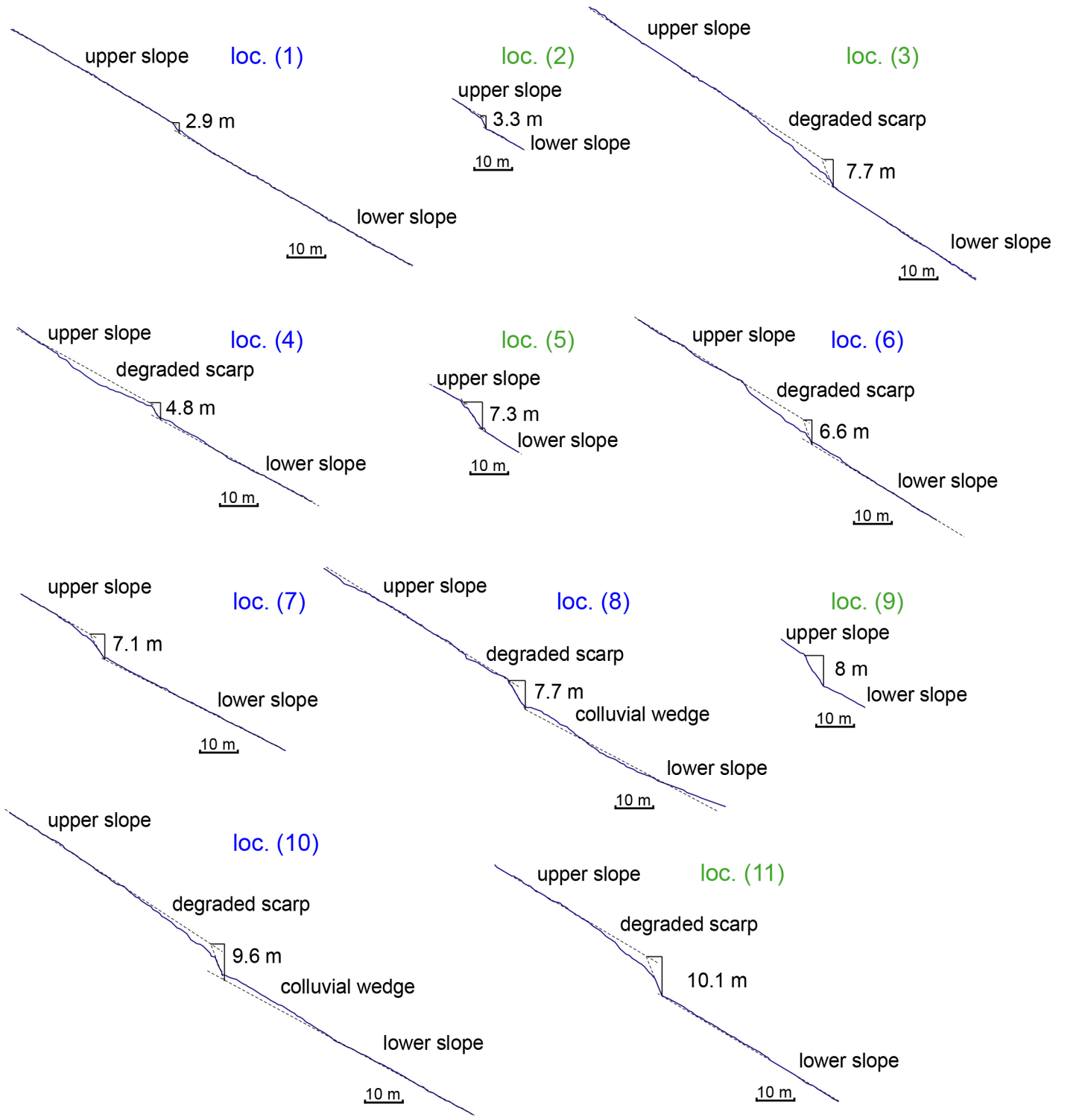
upper slope
loc. (1)
2.9 m
lower slope
10 m
loc. (2)
upper slope
3.3 m
lower slope
10 m
upper slope
loc. (3)
degraded scarp
7.7 m
lower slope
10 m
upper slope
loc. (4)
degraded scarp
4.8 m
lower slope
10 m
loc. (5)
upper slope
7.3 m
lower slope
10 m
upper slope
loc. (6)
degraded scarp
6.6 m
lower slope
10 m
upper slope
loc. (7)
7.1 m
lower slope
10 m
upper slope
loc. (8)
degraded scarp
7.7 m
colluvial wedge
lower slope
10 m
loc. (9)
upper slope
8 m
lower slope
10 m
upper slope
loc. (10)
degraded scarp
9.6 m
colluvial wedge
lower slope
10 m
upper slope
loc. (11)
degraded scarp
10.1 m
lower slope
10 m

(a)

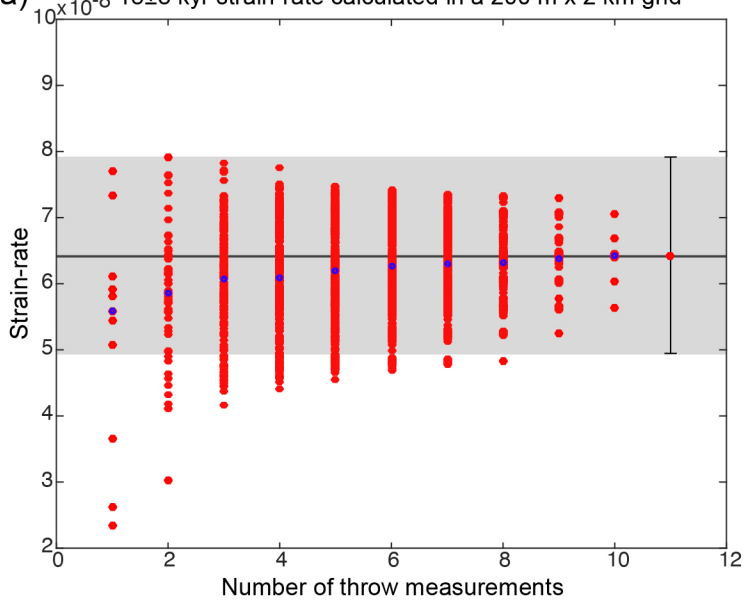
x10-8 15±3 kyr strain-rate calculated in a 200 m x 2 km grid
Strain-rate
Number of throw measurements


N
1 km

(b)

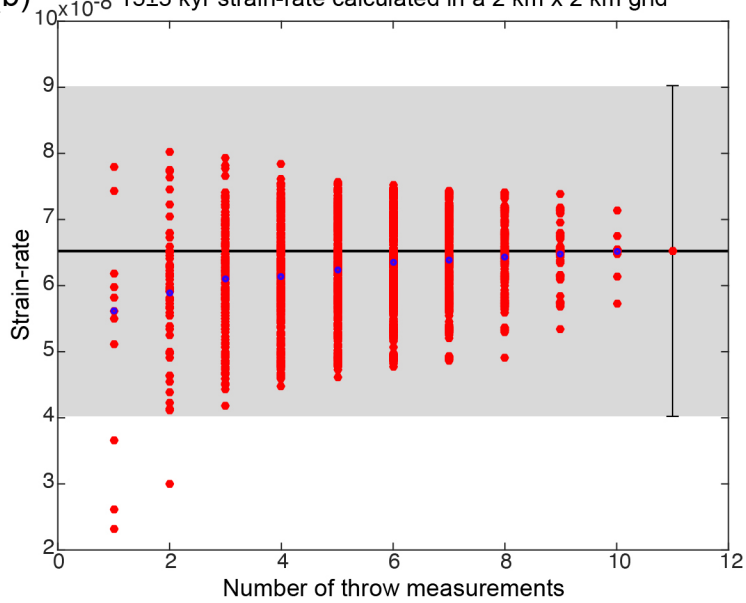
x10-8 15±3 kyr strain-rate calculated in a 2 km x 2 km grid
Strain-rate
Number of throw measurements

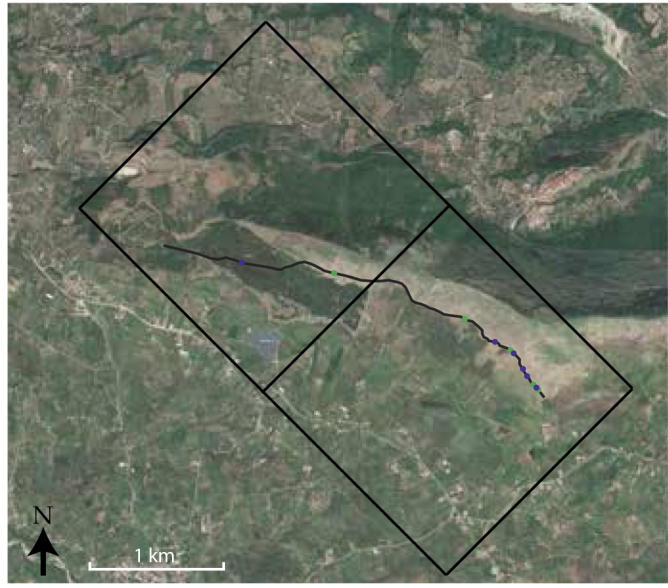
N
1 km

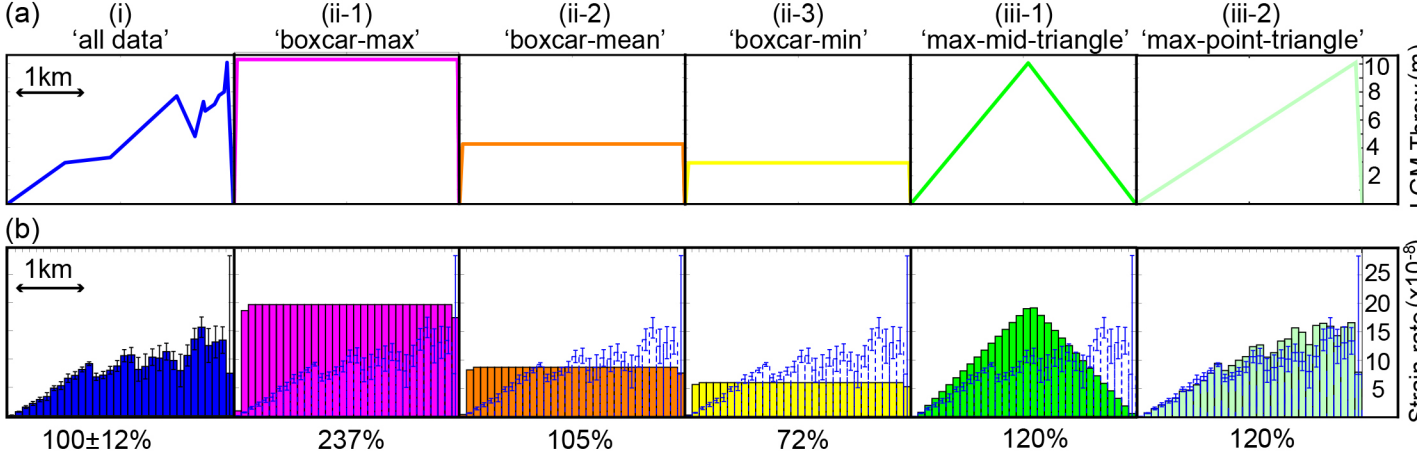
(a)
(i)
'all data'
(ii-1)
'boxcar-max'
(ii-2)
'boxcar-mean'
(ii-3)
'boxcar-min'
(iii-1)
'max-mid-triangle'
(iii-2)
'max-point-triangle'
1km
10
8
6
4
2
LGM Throw (m)
(b)
1km
25
20
15
10
5
Strain-rate (x10-8)
100±12%
237%
105%
72%
120%
120%